ULTRAFAST DYNAMICS OF ELECTRONS AND PHONONS IN GRAPHITIC MATERIALS

by

IOANNIS CHATZAKIS

M.Sc., University of Crete, 2004

AN ABSTRACT OF A DISSERTATION

Submitted in partial fulfillment of the requirements for the degree

DOCTOR OF PHILOSOPHY

Department of Physics
College of Arts and Sciences

KANSAS STATE UNIVERSITY
Manhattan, Kansas

2009

Abstract

This work focuses on the ultrafast dynamics of electrons and phonons in graphitic materials. In particular, we experimentally investigated the factors which influence the transport properties of graphite and carbon nanotubes. In the first part of this dissertation, we used Time-resolved Two Photon photoemission (TR-TPP) spectroscopy to probe the dynamics of optically excited charge carriers above the Fermi energy of double-wall carbon nanotubes (DWNTs). In the second part of this study, time-resolved anti-Stokes Raman (ASR) spectroscopy is applied to investigating in real time the phonon-phonon interactions, and addressing the way the temperature affects the dynamics of single-wall carbon nanotubes (SWNTs) and graphite.

With respect to the first part, we aim to deeply understand the dynamics of the charge carriers and electron-phonon interactions, in order to achieve an as complete as possible knowledge of DWNTs. We measured the energy transfer rate from the electronic system to the lattice, and we observed a strong non-linear increase with the temperature of the electrons. In addition, we determined the electron-phonon coupling parameter, and the mean-free path of the electrons. The TR-TPP technique enables us to measure the above quantities without any electrical contacts, with the advantage of reducing the errors introduced by the metallic electrodes.

The second investigation uses time-resolved ASR spectroscopy to probe in real time the G-mode non-equilibrium phonon dynamics and the energy relaxation paths towards the lattice by variation of the temperature in SWNTs and graphite. The lifetime range of the optically excited phonons obtained is 1.23 ps to 0.70 ps in the lowest (cryogenic temperatures) and highest temperature limits, respectively. We have also observed an increase in the energy of the G-mode optical phonons in graphite with the transient temperature. The findings of this study are important since the non-equilibrium phonon population has been invoked to explain the negative differential conductance and current saturation in high biased transport phenomena.

ULTRAFAST DYNAMICS OF ELECTRONS AND PHONONS IN GRAPHITIC MATERIALS

by

IOANNIS CHATZAKIS

M.Sc., University of Crete, 2004

A DISSERTATION

Submitted in partial fulfillment of the requirements for the degree

DOCTOR OF PHILOSOPHY

Department of Physics
College of Arts And Sciences

KANSAS STATE UNIVERSITY
Manhattan, Kansas

2009

Approved by:

Co-Major Professor
Patric Richard

Approved by:

Co-Major Professor
Itzak Ben-Itzhak

Copyright

Abstract

This work focuses on the ultrafast dynamics of electrons and phonons in graphitic materials. In particular, we experimentally investigated the factors which influence the transport properties of graphite and carbon nanotubes. In the first part of this dissertation, we used Time-resolved Two Photon photoemission (TR-TPP) spectroscopy to probe the dynamics of optically excited charge carriers above the Fermi energy of double-wall carbon nanotubes (DWNTs). In the second part of this study, time-resolved anti-Stokes Raman (ASR) spectroscopy is applied to investigating in real time the phonon-phonon interactions, and addressing the way the temperature affects the dynamics of single-wall carbon nanotubes (SWNTs) and graphite.

With respect to the first part, we aim to deeply understand the dynamics of the charge carriers and electron-phonon interactions, in order to achieve an as complete as possible knowledge of DWNTs. We measured the energy transfer rate from the electronic system to the lattice, and we observed a strong non-linear increase with the temperature of the electrons. In addition, we determined the electron-phonon coupling parameter, and the mean-free path of the electrons. The TR-TPP technique enables us to measure the above quantities without any electrical contacts, with the advantage of reducing the errors introduced by the metallic electrodes.

The second investigation uses time-resolved ASR spectroscopy to probe in real time the G-mode non-equilibrium phonon dynamics and the energy relaxation paths towards the lattice by variation of the temperature in SWNTs and graphite. The lifetime range of the optically excited phonons obtained is 1.23 ps to 0.70 ps in the lowest (cryogenic temperatures) and highest temperature limits, respectively. We have also observed an increase in the energy of the G-mode optical phonons in graphite with the transient temperature. The findings of this study are important since the non-equilibrium phonon population has been invoked to explain the negative differential conductance and current saturation in high biased transport phenomena.

Table of Contents

List of Figures

List of Tables

Acknowledgements

First of all, I would like to thank Prof. Theo J. M. Zouros for trusting my skills and giving me the opportunity to study physics at Kansas State University. Unfortunately, we did not have the chance to work together for a long period. He is one of the best teachers and passionate researchers I have ever met. I used to call him teacher, and I will always do.

I would also like to thank my major advisor Prof. Patrick Richard for his guidance and support during my PhD thesis. We had fruitful and long discussions together, even by phone across the states! He was the one who believed in me more than anybody else, giving me the opportunity to make my dream come true. I will always be grateful for his support throughout the years. His love for physics and his skills in understanding people make him the ideal supervisor. I feel very lucky to be one of his students. Actually, I was his last graduate student, since after a long and successful career he then retired.

Furthermore, I would like to thank Prof. Tony F. Heinz, who accepted me as a visiting graduate student at Columbia University in order to perform some experiments as part of this thesis. Even though he is very busy, I was always welcome in his office. He was patient and explanatory with solutions to overcome various problems. Instead of giving me a direct solution, he was triggering my mind with questions that pointed me to the right path.

Moreover, I thank Prof. Itzik Ben-Itzhak who acted as a titular advisor for this thesis. He agreed to do so a few months before the graduation, though we never worked together and thus he had to trust my skills. I also thank Prof. Zenghu Chang's group for their support and especially Hiroki Mashiko for helping me to have a good laser beam profile and for our fruitful discussions about science. In addition, I thank all J.R. Macdonald Laboratory and Prof. T. Heinz's group members, at Kansas State University and Columbia University, respectively, for their support and friendly manners.

At this point I would like to thank my family who made me the person I am today. I will be always grateful to them! I also thank Vallia's family for being close to me these years even by the phone across the ocean.

Last but not least, from the deepest of my heart, I thank my wife Vallia. She was always there for me, and this thesis is our success. When we work together, we are a very good and strong team and this is amazing. I will always be grateful to you, Vallia!

Dedicated

To my wife Vallia for her endless love and support all these years…

CHAPTER 1 - Introduction

The discovery of multi-wall carbon nanotubes formed in a carbon arc discharge by Sumio Iijima in 1991 at NEC Corporation had an enormous impact on the condensed matter and materials science fields of nanoscale science and electronics. In his *Nature* publication [1], Iijima reported on the preparation of a new type of finite cylindrical carbon structure. In particular, he cited that the formation of these tubes, ranging from a few to a few tens of nanometers in diameter, suggested that engineering of carbon structures should be possible on scales considerably greater than those relevant to the fullerenes.

Graphene is a single layer of carbon atoms densely packed in a honeycomb crystal lattice [2]; thus carbon nanotubes can be thought of as graphene sheets rolled up into nanometer-sized cylinders. Novoselov *et al*. [2] showed that graphene could be isolated from graphite simply using adhesive tape. The many exotic features which graphene presents are due to linear dispersion of the electronic bands with the momentum, near to Dirac-points where the conduction and the valence bands cross. The electrons can be described as though they are massless particles similar to photons [3].

Nowadays, these graphitic materials seem to have unlimited potential, and further breakthroughs in fundamental physics are expected. For example, carbon nanotubes are stronger and at the same time lighter than steel, they have exceptional thermal properties, while they demonstrate semiconducting or metallic properties depending on their structure. They have low production cost and are relatively easy to grow. In addition, due to their excellent optical properties, it is expected that making both electronic and optoelectronic devices from the same material will become possible [4]. Thus, interest has grown in the potential applications of carbon nanotubes, ranging from – but not limited to – optics, electronics, materials science, and biotechnology.

For power transmission or high performance electronics, the ability of materials to carry current is fundamental and of high importance. However, there are mechanisms which restrict the performance of the materials. For example, the dominant mechanism which limits the conductivity is the scattering of electrons by phonons or by impurities.

At room temperature and at low bias, it is has been suggested that the origin of the resistivity is the scattering of electrons from acoustic phonons [38]. At high biases, electrons gain enough energy (e.g. > 0.2 eV) to emit optical phonons, which results in very effective scattering. Several groups have extensively investigated this kind of scattering and they have found that the current saturation and the negative differential conductance are due to the non-equilibrium optical phonons [29,40,44,]. Lazzeri *et al.* [43] have shown that at the above conditions the resistivity strongly depends on the optical phonon thermalization time. In other words, the lifetime of the phonons reflects the phonon coupling with a thermal bath. Thus, by increasing the phonon coupling with a thermalized source, the performance of the nanotubes increases drastically. Therefore, the measurement of the decay-time of the non-equilibrium phonons is of fundamental importance. Parallel to that, the dynamics of the optically excited states in nanotubes play a decisive role in the electronic devices. By measuring the electron-electron and electron-phonon interaction scattering times we can determine the timescale in which the energy of the excited electrons is lost.

The above interactions (i.e. electron-phonon and phonon-phonon) strongly influence the conductivity of the materials. These procedures are very sensitive to temperature and in addition to the above we address the response of the nanotubes and graphite under different temperatures.

Ultrafast dynamics of electronic excitations and decay processes in carbon nanotubes and graphite materials are studied in this thesis. The study of these processes is made possible by the use of ultafast femtosecond laser pulses. This study is divided into two parts: the first was conducted in the James R. Macdonald Laboratory of the Kansas State University physics department. The detection and time history of the events were measured with an apparatus equipped to perform Time-Resolved Two-Photon Photoemission (TR-TPP) spectroscopy. In particular, the energy transfer rate from the optically excited electronic system to the lattice, and the electron-phonon coupling have been estimated. In addition, the mean free path of electrons in double-wall carbon nanotubes have been measured. The second part of this work was performed at the Nanoscale Science and Engineering Center at Columbia University. Time Resolved Anti-Stokes Raman spectroscopy has been applied in order to measure the temperature dependence of the decay dynamics of optically excited phonons in carbon nanotubes and graphite. More specifically, the relaxation rate $1/\tau$ of the G-mode in these graphitic materials at different temperatures has been measured.

Estimating the energy relaxation rate, the electron-phonon coupling, the electron mean free path, and the optical phonons decay rate are of high importance in understanding the restrictions and overcoming the barriers which limit the performance of the carbonic materials as fundamental components in electronic devices.

The structure of this dissertation is as follows: Chapter 2 gives a description of the current understanding of the structural parameters of carbon nanotubes, and in particular a description of the electronic structure and phonon dispersion relations. The following two chapters present observational results. Chapter 3 presents the first part of the thesis project, which is the study of the electron dynamics in double-wall carbon nanotubes (DWNTs). The experimental setup and the TR-TPP spectroscopic technique used in this part of the work are described in detail. Chapter 4 presents the observation of temperature dependence of the G-mode optical phonons in carbon nanotubes and graphite. An analytic description of the experiment and the method applied for this study (i.e., Time Resolved Anti-Stokes Raman spectroscopy) are also given. A brief summary of results is given in Chapter 5, while more details for various parts of the analysis are given in the Appendices at the end of this dissertation.

CHAPTER 2 - Structure of Carbon Nanotubes

2.1 Introduction

A tube made of a single graphite layer (graphene) rolled up into a hollow cylinder is called single-wall carbon nanotube (SWNT). Many concentrically arranged nanotubes are referred to as multi-wall carbon nanotubes (MWNTs). At the surface of the tube the carbon atoms are organized in a honeycomb lattice. The coordination number is 3 and the surface curvature induces some sp^3 hybridization in addition to the sp^2, which is typical to graphene. Moreover, carbon nanotubes are one-dimensional systems with translational periodicity along the tube axis.

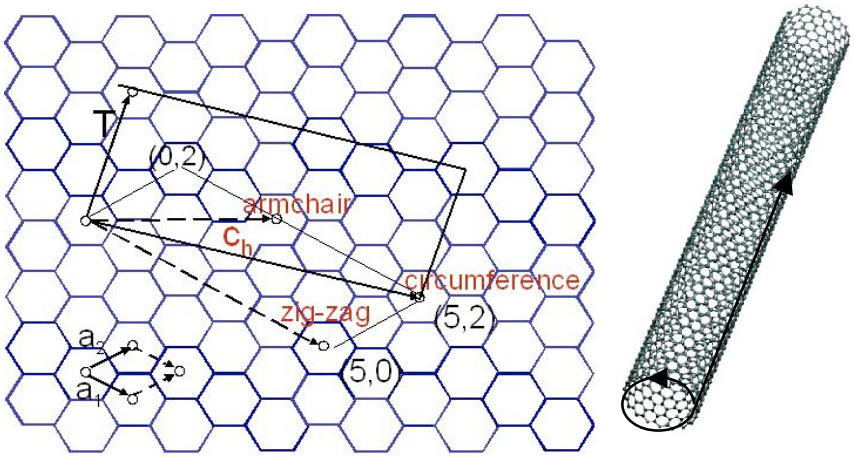

Figure 2.1 Graphene honeycomb lattice with the lattice vectors $\mathbf{a}_1$, $\mathbf{a}_2$. The chiral and the translation vector form a rectangle, which is the unit cell of the tube. These two vectors are highlighted on the tube on the right [5-7].

Different diameters and microscopic structures of carbon nanotubes (CNTs) can be achieved based on the way the sheet of graphene has been wrapped to form a cylinder. These are defined by the chiral angle, which is angle of the hexagon helix around the tube axis. Many of the properties of MWNTs are very close to those of the graphite, since the latter is made of many sheets of graphene connected to each other by Van Der Waals forces.

The nanotubes are usually labeled in terms of graphene lattice vectors because they are closely related materials. The graphene sheet is wrapped such that the graphene lattice vector $\mathbf{C}_h = n_1\mathbf{a}_1+n_2\mathbf{a}_2$ (see Figure 2.1) becomes the circumference of the tube. The vectors $\mathbf{a}_1$, $\mathbf{a}_2$ are unit vectors and connect two equivalent points. This chiral vector uniquely defines each nanotube and it is denoted by the pair of integers n_1 and n_2. The angle between $\mathbf{C}_h$ and $\mathbf{a}_1$ is called the chiral angle and gives the direction of $\mathbf{C}_h$. It is given by the formula

$$\theta = \tan^{-1}\left[\sqrt{3}\frac{n_2}{n_2+2n_1}\right] \tag{2.1}$$

Characteristic parameters of the nanotubes are the length of $\mathbf{C}_h$, the translation period $\mathbf{T}_{tr}$ of the circumference along the tube axis, and its diameter d, which are given by equations (2.2) to (2.4), respectively.

$$C_h = \sqrt{3}a_{c-c}\sqrt{(n_1)^2+n_1n_2+(n_2)^2} \tag{2.2}$$

$$\mathbf{T}_{tr} = -\frac{2n_2+n_1}{nR}\mathbf{a_1}+\frac{2n_1+n_2}{nR}\mathbf{a}_2 \tag{2.3}$$

$$d = \frac{|\mathbf{C}_h|}{\pi} \tag{2.4}$$

In the above equations $a_{c\text{-}c}$ is the carbon bond length, n is the highest common divisor of (n_1,n_2), and $R = 3$ if $(n_1\text{-}n_2)/3n$ is integer or $R = 1$ otherwise.

The unit cell is formed by a cylindrical surface with length T_{tr} and diameter d. The number of atoms in the unit cell is then given by the formula

$$q = \frac{S_t}{S_g} = \frac{2\left(n_1^2 + n_1 n_2 + n_2^2\right)}{nR} \tag{2.5}$$

where the S_t is the area of the cylinder surface and S_g is the area of the hexagonal graphene unit cell.

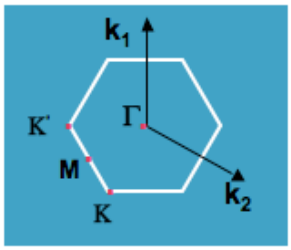

Figure 2.2 Brillouin zone of the graphene with the high-symmetry points K, Γ and M. The reciprocal lattice vectors $\mathbf{k}_1$, $\mathbf{k}_2$ in Cartesian coordinates are $\mathbf{k}_1 = (0,1)4\pi/\sqrt{3}a_0$ and $\mathbf{k}_2 = (0.5\sqrt{3},-0.5)4\pi/\sqrt{3}a_0$.

Since the graphene unit cell contains two carbon atoms, there are $n_c = 2q$ carbon atoms in the unit cell of the nanotube. The nanotubes are divided in three categories depending on the integers n_1, n_2: Armchair (n,n), Zig-Zag $(n,0)$ and Chiral (n_1,n_2). In the first two categories they exhibit metallic or semiconducting behavior, respectively. If $(n_2\text{-}n_1)/3$ is an integer they have metallic behavior, otherwise semiconducting. The Brillouin zone (BZ) of graphene is displayed in Figure 2.2.

2.2 Electronic structure of Carbon Nanotubes

For simplicity we will first study the electronic structure of graphene and then present some differences between graphene and the carbon nanotubes. The electronic structure of the latter can be studied by using the tight binding approximation Linear Combination of Atomic Orbitals (LCAO). The basic bonding of the carbon atoms involves the formation of sp^2 hybridized atomic orbitals. These lead to the 3-fold coordination in the graphene lattice and the corresponding σ bonds. The additional electron for each carbon atom is in a p_z orbital. These interact to form the π-electron system of graphene, which controls all the electronic and optical properties to be discussed in this thesis. Due to sp^2 hybridization the carbon nanotubes have two types of bonds, the σ and π. The σ bonds are in the lattice plane and they are very strong, but their energy is far away from the Fermi level, so there is not any contribution to the conductivity or absorption of light. In contrast, the π and π^* orbital are perpendicular to the lattice plane, thus normal to the plane of σ, and they are responsible for the above electronic properties.

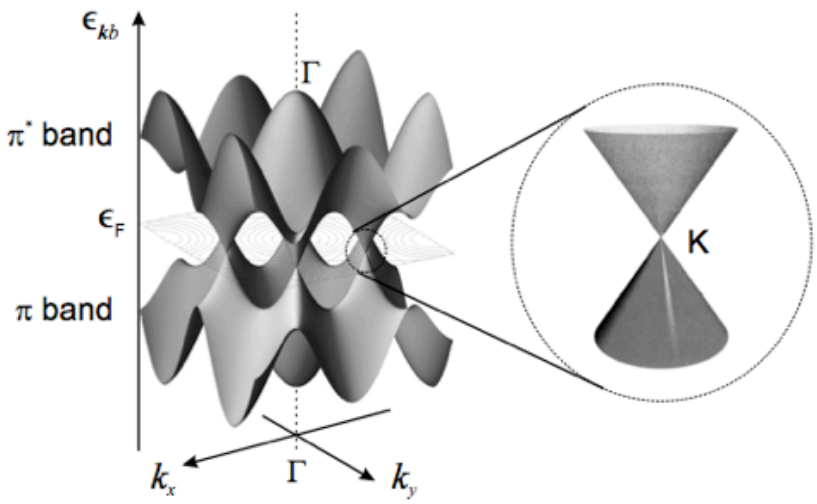

Figure 2.3 Energy dispersion $E(k_x,k_y)$ of graphene. The K, K΄ are the crossing points of the bands π and π^* and have conical shape. The π band is completely filled in the ground state and π^* completely empty [8].

The π and π^* cross the Fermi level at the K, K′ points of the BZ in a way which forms six cones with reflection symmetry with respect to the Fermi level (see Figure 2.3). These six distinct points define the Fermi surface, which is responsible for the metallic or semiconducting behavior of the nanotubes. The bands close to the Fermi level are linear [5].

A starting point to describe the π-electron system we use is the Schrödinger equation in the form [7]

$$\widehat{H}\Psi = E\Psi \tag{2.6}$$

where $$H = \begin{pmatrix} \varepsilon_p & -\gamma_0 f(x,y) \\ -\gamma_0 f^*(x,y) & \varepsilon_p \end{pmatrix},$$

$$f(k_x,k_y) = \sqrt{1+4\cos(\frac{\sqrt{3}ak_x}{2})\cos(\frac{ak_y}{2})+4\cos^2(\frac{ak_y}{2})},$$

and $a = 2.461\,\text{Å}$, with properly chosen wave functions to satisfy the above relation. One of the favorable hybridizations of carbon is the sp^2 type where a 1*s* and two 2*p* atomic wavefunctions are combined in order to form the hybridized. The electronic wave functions $\Phi_l(\mathbf{k},\mathbf{r})$ can be approximated as a linear combination of the atomic wave functions $\psi_l(\mathbf{r}-\mathbf{R_A})$

$$\Phi_l(\mathbf{k},\mathbf{r}) = \frac{1}{\sqrt{N_0}}\sum_{\mathbf{R_A}}^{N_0} e^{i\mathbf{k}\cdot\mathbf{R_A}}\psi_l(\mathbf{r}-\mathbf{R_A}) \tag{2.7}$$

where N_0 the number of the unit cell in the crystal, $\mathbf{R_A}$ the lattice vectors and *l* denotes the atomic orbital. The $\Phi_l(\mathbf{k},\mathbf{r})$ are the eigenfunctions of the unperturbed Hamiltonian, which satisfy the Bloch theorem $\Phi_l(\mathbf{k},\mathbf{r}+\mathbf{R}) = e^{i\mathbf{k}\cdot\mathbf{R}}\Phi_l(\mathbf{k},\mathbf{r})$. The eigenfunctions of the total Hamiltonian $H = H_0 + H_{int}$ can be expressed as

$$\Psi(\mathbf{k},\mathbf{r}) = \sum_l C_l(\mathbf{k})\Phi_l(\mathbf{k},\mathbf{r}) \tag{2.8}$$

which solve the eigenvalue problem, described by the equation (2.6). Equation (2.6), in combination with equations (2.7) and (2.8), gives the energy eigenvalues [7]

$$E = \varepsilon_{2p} \pm \gamma_0 \sqrt{1 + 4\cos(\frac{\sqrt{3}ak_x}{2})\cos(\frac{ak_y}{2}) + 4\cos^2(\frac{ak_y}{2})} \tag{2.9}$$

where γ_0 represents the interactions (i.e. the perturbation) between the two π electrons and takes values between 2.7 eV and 3.1 eV, $\mathbf{k}$ is the electronic wave vector for the graphene BZ and a is the lattice vector length.

2.2.1 The zone folding approximation

The zone folding approximation is suitable for understanding the electronic properties of SWNTs from the electronic structure of graphene. The basic assumption of this approximation is that the curvature effects of the tube do not play an important role for the electronic properties and it is applicable for nanotubes with diameters $>$ 1nm.

Since the length of the nanotubes is several orders of magnitude larger than their diameters, they can be considered as one-dimensional solids. The electrons or phonons can have quantized states along the circumference $\mathbf{C}_h$ of the nanotubes and continuum spectrum in the z-axis, which is the axis of the cylinder. The quantization condition is

$$\mathbf{k}\cdot\mathbf{C}_h = \mathbf{k}_\perp\cdot\mathbf{C}_h = 2\pi m \Rightarrow |\mathbf{k}_\perp| = \frac{2\pi}{\lambda} = m\frac{2\pi}{|\mathbf{c}|} = m\frac{2}{d} \tag{2.10}$$

$$\mathbf{k}_\perp\cdot\mathbf{T}_{tr} = 0$$

and for the $\mathbf{k}_z$

$$\mathbf{k}_z\cdot\mathbf{C}_h = 0 \qquad \text{and} \qquad \mathbf{k}_z\cdot\mathbf{T}_{tr} = 2\pi$$

where **k** is the wavevector (with $\mathbf{k}_\perp$, $\mathbf{k}_z$ perpendicular and parallel to the tube axis, respectively), *d* is the diameter, and *m* is an integer number which represents the number of wavelengths which fit in the circumference of the tube. The values of *m* are $-q/2+1,\ldots 0,1\ldots,q/2$. Specifically, the wave function of the electron or the phonon needs to have 2π phase shift, around the circumference, otherwise it will interfere destructively. The result of this construction is that nanotubes can be either metals or semiconductors depending on their indices (n_1,n_2). If the K point (the crossing of π , π^* energies) is included from one of the allowed **k** lines, then the nanotube is metallic, otherwise it is semiconducting (Figure 2.4).

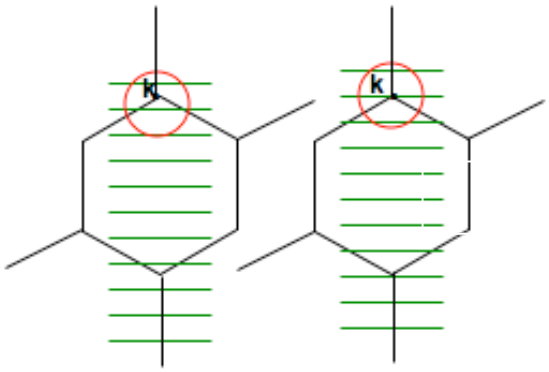

Figure 2.4 The BZ for semiconducting (left) and metallic (right) nanotubes. The green lines are the allowed wavevectors. In the left panel there is not any cutting line (k) passing from the point K, and thus BZ belongs to the semiconducting type of nanotubes. In contrast, in the right panel there is a k line, which passes from the K point and the nanotube belongs to metallic type.

The maximum $|\mathbf{k}_\perp|$ follows from the number of atoms ($2q$). Then the first BZ is divided in *q* lines parallel to the z-axis separated by $|\mathbf{k}_\perp| = 2/d$ and $k \in (-\pi/a, \pi/a]$ [5,6]. Each one of

these lines corresponds to a sub-band. The energies of these sub-bands are given from the relation $E = E_0 + \frac{\hbar^2 k^2}{2m^*}$, which implies a whole spectrum of distinct states that in turn gives a distinct density of states (DOS) spectrum. Generally the DOS is given by $n = c_d E^{(d-2)/2}$ [9], where c_d is a constant and d is the dimension of the space. For one-dimension system like the nanotubes, the DOS is $\sim 1/\sqrt{E}$ [10]. The spikes of the DOS are called Van-Hove singularities and they are the points where the group velocity is zero (Figure 2.5).

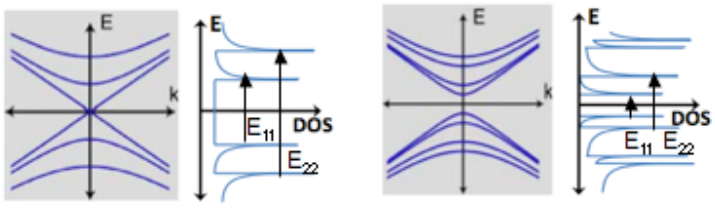

Figure 2.5 The band structure and the density of states (DOS) for metallic (left) and semiconducting (right) nanotubes (adopted from [73]).

It is instructive to pay closer attention to the density of states (DOS), an important quantity for the study of the electronic properties of any material. The density of states *n(E)* of the nanotubes is given by [10]

$$n(E) = \frac{4a_0}{\pi^2 d\gamma_0} \sum_{m=-\infty}^{\infty} g(E, E_m) \qquad (2.11)$$

where γ_0 is the interactions integral, d is the diameter of the tube, $a_0 = 2.461$ Å and

$$g(E, E_m) = \begin{cases} |E| / \sqrt{E^2 - E_m^2} & \text{if } |E| > |E_m| \\ 0 & \text{if } |E| < |E_m|. \end{cases}$$

The $g(E, E_m)$ for $E_m \neq 0$ shows a divergence at $E = E_m$ as expected for a particular point of a one-dimensional system. The density of states is a characteristic difference between graphene (2-D system) and nanotubes.

At this point it is worth mentioning that the optical excitations in nanotubes demonstrate an excitonic character, which means that the optical transitions, e.g., E_{11} and E_{22}, are excitons governed by electric-dipole selection rules [11].

CHAPTER 3 - Electron dynamics in double-wall carbon nanotubes

3.1 Introduction

The carbon nanotubes have been established as one of the most promising components for electronic transport and high performance electronics. SWNTs have been shown to sustain current densities exceeding 10^7 A/cm^2 before damage [12,29]. This property makes SWNTs promising material for interconnects. It is known that the resistance $\rho = h/(2e^2)(1/nl)$ is inversely proportional to the number of tubes n and the mean free path l and h the Plank constant [74]. Therefore, the conductance can be increased by a factor which is equal to the number of shells. One can also use MWNTs, but these systems are more difficult to describe. DWNTs can be considered a limiting case of MWNTs and as such they are of prime interest to researchers. On the basis of their inner and outer (I-O) wall types, DWNTs can be classified into four groups: semiconducting-semiconducting (S-S), semiconducting-metallic (S-M), metallic-semiconducting (M-S), and metallic-metallic (M-M). These types of nanotubes could have diverse uses in nanoscale devices. Therefore, it is essential to correctly quantify the electron mean-free path, l, of DWNTs, a crucial parameter in transport phenomena.

The conductivity of MWNTs has been extensively investigated in transport measurements, where the observed values of l varied widely from 0.1 to a few microns or even greater. This range is most probably due to a combination of factors, such as variations in contact resistance at the nanotubes-electrode junctions and unknown distribution of current density among different tubes. When the DWNT is placed between the two electrodes, the electric current will be determined by the nature of the contacts and the intrinsic conductivity. The scattering rate of electrons between the metal and the nanotube can be expressed through the Fermi rule, where the coupling operator is proportional to the length of the conducting area, the geometry and the configuration between the nanotube and the electrodes: end or side contacts effects [13]. This combination of different factors introduces difficulties in accurate evaluation of the conductance.

In an alternative to transport measurements, we use a non-contact approach for studying the conductivity parameters of DWNTs. This alternative method probes the temporal evolution of the electronic excitations in the vicinity of the Fermi level, E_F. In this work a direct measurement of the electron-phonon (e-ph) energy transfer rate for DWNT at room temperature and its dependence on the electron and lattice temperatures T_e and T_l, respectively, are presented. The energy transfer rate can be obtained by probing the dynamics of the excited electrons above the Fermi level following excitation by a femtosecond laser pulse. The rate at which the energy is exchanged depends on the e-ph coupling, which in turn is directly related to the mass-enhancement parameter λ. This parameter is a factor by which the effective mass of an electron is changed due to e-ph interactions. More details about λ are given in Section 4.2.4 and appendix B. By analyzing the dynamics of the electrons one can determine λ. Applying the theory of Allen [14] we calculate the e-ph scattering time and then the mean free path. We use femtosecond TR-TPP spectroscopy [30] to carry out these measurements [15,16].

The TR-TPP method enables us to study the relaxation dynamics of the charge carriers on a femtosecond timescale with very high resolution of about 10 meV for detected ~1 eV electrons. In this experiment we were able to determine the temperature dependence of the energy transfer rate, H, from the excited electronic system to the lattice, which has been derived by differentiating the time evolution of the internal energy with respect to time.

The reported experimental values of the electron mean-free path for SWNTs are 15 μm [15]. Experiments using the TR-TPP technique have shown that the electron-electron (e-e) scattering time strongly increases as the carrier energies approach the Fermi level [17-19]. The e-e scattering times are becoming extremely short, few tens of femtosecond or less, as the carrier energies are far above the Fermi level. However, the temperature dependence of the energy transfer rate yields a small mass-enhancement parameter λ of 0.0004 ± 0.0001 for SWNTs [15], which is directly related with the electron-phonon coupling [15]. Details about the mass enhancement parameter are given in appendix B. We infer the mean free path, l, and the intrinsic conductivity by measuring the e-ph scattering time $\tau(E)$, which along with impurity effects is the dominant mechanism for the resistance in metals [17,18]. In our experiment for DWNTs we find a mass enhancement parameter ($m = m_0(1+\lambda)$, see appendix B) of $\lambda = (1.16 \pm 0.16) \times 10^{-4}$. This

value of λ gives us at room temperature an e-ph scattering time of 25 ± 1 ps. By multiplying this time with the Fermi velocity v_F (10^8 cm/sec) we then infer a mean free path of 25 ± 1 μm.

In this project we would also have liked to confirm the Fermi-Liquid Theory (FLT), i.e. that $\tau \propto (E-E_F)^{-2}$ [15-17,19]. However, this was impossible with the current experimental conditions (see below section 3.2.2).

3.2 Experimental

3.2.1 Samples and Ultra High Vacuum system

DWNT samples of high-purity (>95%) produced by the chemical vapor deposition (CVD) method were used in the present study. The experimental medium consisted of 0.4 mm thick freestanding DWNT ‘‘bucky’’ paper, with the outer diameter of the nanotubes of 4 ± 1 nm. To prepare the BuckyPaper sheet, nanotubes are suspended in a fluid, and then filtered onto a membrane support. After drying, the paper is removed from the support, leaving a freestanding paper. Standard BuckyPaper is ~50% dense, and it can be tailored for particular applications. The sample was attached to a Tantalum (Ta) substrate and outgassed in multiple heating and annealing cycles with a peak temperature of 700 K. The sample temperature was measured using a thermocouple attached on the Ta disk. Figure 3.1 shows the configuration of the sample holder. The position of the sample within the chamber was controlled with a linear feedthrough manipulator. This configuration gives the option to change the position of the laser spot on the sample. Ultra-high vacuum (UHV) of typically 10^{-10} mbar was maintained by a combination of a roughing-pump and a turbo-molecular pump.

Figure 3.1 Sample holder-heater. The white color cables are used to provide the power for the heater, which consists of a plate of Ta. The shiny wires beneath the Ta frame are connected to the thermocouple. The black material in the middle of the frame is the sample (bucky paper) of DWNTs.

3.2.2 Laser system and optics for time-resolved spectroscopy

The laser system, used in this experiment, is a homemade light source.Femtosecond laser pulses at 790 nm are generated by a Ti:Sapphire oscillator and subsequently amplified to reach an energy of 2.5 mJ per pulse and a duration of ~ 25 fs. The 10 fs seed pulse with nanojoule energy is stretched to 100 ps by a pair of gratings (stretcher) in order to avoid damaging the laser amplification medium, which is a crystal of Ti:Sapphire. After the amplification, the energy of the pulse is around 5 mJ with 30 ps duration. Subsequently the pulse is compressed to ~25 fs by sending it through another pair of gratings (compressor). The chirp, which has been introduced during the stretching, has been removed during the opposite procedure, the compression. At this final stage the energy, which has been reached, is 2.5 mJ per pulse. The repetition rate of the laser system is 1 kHz. Our experimental setup was located in a different room than the laser source, and evacuated transport lines were used in order to guide the laser radiation to the experimental table.

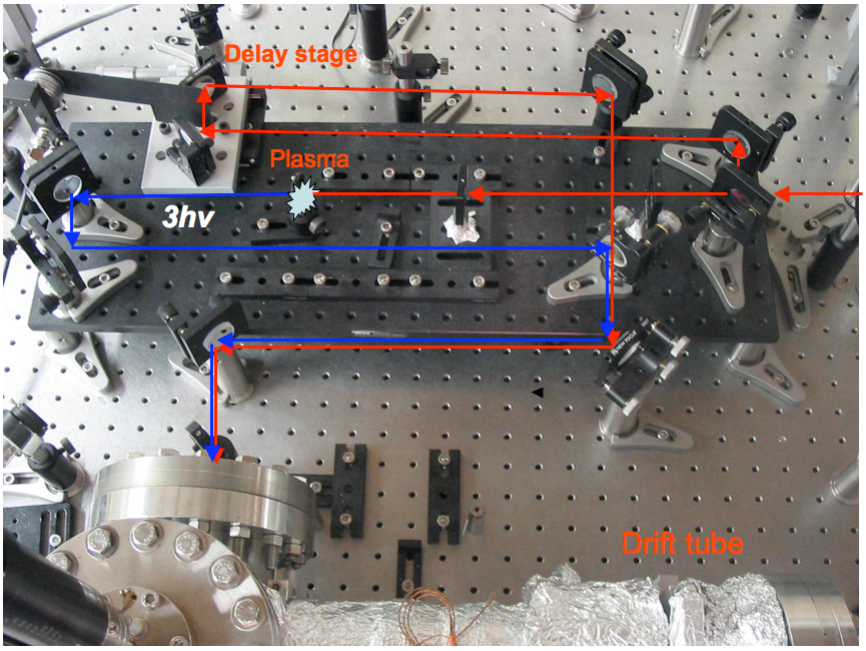

Figure 3.2 The optical setup for the time-resolved photoelectron spectroscopy. The red lines show the paths of the excitation beam (IR radiation at 790 nm), while the blue lines represent the beam used to probe the excited states (UV at 263 nm). The chamber, which contains the time-of-flight tube, is on the bottom of the picture. At the end of the chamber (right side) there is a flange, which supports the detector.

The linear polarization of the 790 nm beam is controlled by a λ/2 waveplate. The initial laser beam is separated into two parts, the pump and the probe beams, with a polarized splitter. The pump beam had s-polarization, in order to suppress the ionization of the electrons due to the pump only, while the probe had p-polarization. The λ/2 waveplate in combination with the polarized splitter was used to control the fluence of the pump beam. The 263 nm UV photons of (probe beam) were produced through non-linear effects during the photoionization of N_2 molecules by focussing the 790 nm beam in air using a 150 mm focal length lens. A second lens with 150 mm focal length was used to collimate the 263 nm beam. Dielectric mirrors have been used in the UV path so as to eliminate the residual of the IR radiation after the tripling of the frequency (see Figure 3.2).

The resulting UV and IR beams were delayed with respect to each other and spatially overlapped on the sample in collinear configuration at 30° incidence angle. The fluences of the IR and UV beams were ~40 μJ/cm^2 and 30 nJ/cm^2, respectively. The 30° angle was introduced in order to prevent the scattered light reaching the detector. A mirror can be flipped into the beams' path in front of the UHV chamber to send the beams onto a mimic sample consisting of a pinhole 100 μm outside of the chamber. The optical path from the last lens of the optical setup to the pinhole was set equal to the optical path from the lens to the surface of the sample. To achieve the spatial overlap of the probe and the pump, both beams were steered through the pinhole.

In order to find the zero-time delay for which the beams (IR-UV) reach the sample simultaneously, the flipped mirror was used to send them through the pinhole setup, with the IR to be primarily focused by a parabolic mirror in the air. This produced a secondary plasma and in turn UV radiation for a second time. The initial and the secondary UV pulses are overlapped in space by passing them through the 100 μm pinhole (mimic sample). The time delay between the two pulses was adjusted by the delay stage until the fringes from the interference were produced and observed due to fluorescence of a screen of paper (see Figure 3.3).

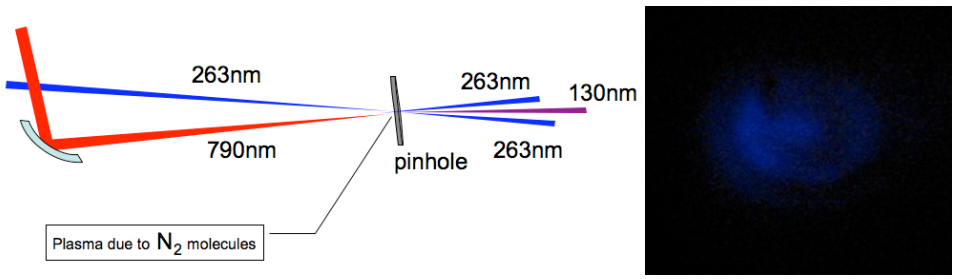

Figure 3.3 Interference fringes of the UV photons 263 nm of the two collimated beams overlapped in the time and space domains.

After finding the zero delay, the parabolic mirror was removed. The optimization of the zero-time delay was further improved by maximizing the photoelectron signal.

One of the main problems that affected our experimental data was vibrations of the laser transfer lines as a result of the very long distance between the laser source and the experimental setup, the laser beam pointing was very sensitive to the vibrations of the transport lines. The spatial overlap of the split and subsequently recombined laser beams was frequently lost, thus making it impossible to get data in the needed long integration times. An additional problem to the first was the drift of the beams in space.

3.2.3 Time-of-flight and photoelectron detection

The principles of a time-of-flight (TOF) spectrometer are very simple [20]. Typical photoemission geometry at a solid surface is sketched in Figure 3.4. Photons with energy $\hbar\omega$ and angle ϑ with respect to the normal on the surface are incident on the sample and photoelectrons are emitted. We can calculate the energy of the electrons by measuring the time t in which the electron flies through distance L. The energy is given by [20] as

$$E = \frac{m}{2}\left(\frac{L}{t}\right)^2 \tag{3.1}$$

where m is mass of the electron. In practice, we do not measure the energy of an individual electron but the distribution of an electron beam having a pulse width Δt. It follows that the relative energy resolution $(\Delta E/E)=[(2\Delta t/t)+ (2\Delta L/L)]^{1/2}$ depends on the resolution Δt and the uncertainty distance ΔL. An accurate estimate of Δt and the length, L, of the drift tube determine the achievable resolution, which is given by the equation,

$$\Delta E = \sqrt{\frac{8E_{kin}^3}{m_e}}\frac{\Delta t}{L} \tag{3.2}$$

where the second term $(2\Delta L/L)^{1/2}$ has been neglected.

Photoelectrons following the photoionization by the UV pulse, drifted into the magnetically shielded and electrically isolated 31 cm long spectrometer tube and were detected with a backgammon position-sensitive detector. The detection of the electrons in our experimental configuration, is not normal to the surface, but rather at 30^{o}. This angle introduces a component in their momentum given by $\hbar k_{\|} = \sqrt{2m_e E}\sin(30)$ where $k_{\|}$ is the parallel component to the sample surface of the electron's momentum. Since the electron's TOF is measured, the energy resolution ΔE of the spectrometer depends on the electron energy. In our case for $E_{\text{kin}} \sim 1$ eV the resolution is around 10 meV. The TOF and the electronic setup are shown below in Figure 3.4.

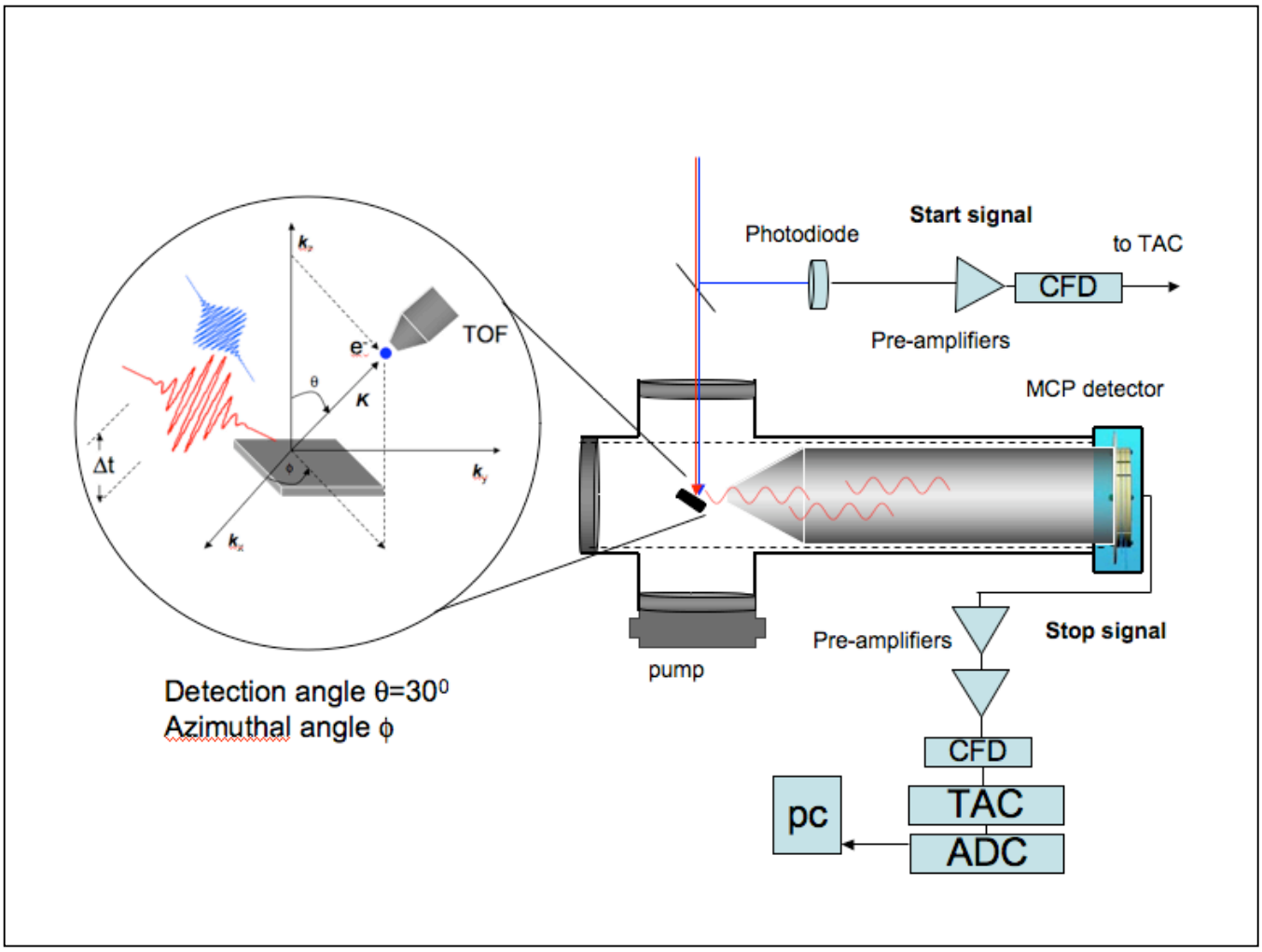

Figure 3.4 The vacuum chamber with the electronics for measuring the time-of-flight of the ionized electrons. The inset describes the geometry of the excitation in more detail. The start signal of the time amplitude converter (TAC) is provided by a photodiode responding to the laser pulse. The stop signal comes from the multi-channel plate (MCP) detector when the electrons arrive. The signals (start and stop) are initially amplified by the pre-amplifiers, then by using constant fractions discriminators the noise is removed, and in turn the time delay between the two signals is converted to a voltage with the TAC. The analog-digital converter (ADC) converts the analog signals in a digital sequence of pulses that are read into the computer.

3.2.4 Time-resolved photoelectron spectroscopy-spectra from DWNTs

We investigate the nature of low-energy excitations in DWNTs by pumping the states using femtosecond infrared laser pulses. The temporal evolution of the population is examined by ionizing the resulting population with delayed femtosecond UV pulses. The TOF of the ionized electrons is recorded for a range of energies above the Fermi energy, E_F, in order to investigate the relaxation dynamics of the charge carriers. The initial fast relaxation is attributed to the internal thermalization of the electronic system, and it is primarily driven by e-e scattering processes. After the system returns to a Fermi-Dirac distribution, it continues to decay with a slower rate associated with electron gas cooling through e-ph interactions. The evolution of non-equilibrium carriers due to the presence of the pump beam is illustrated schematically in Figure 3.5.

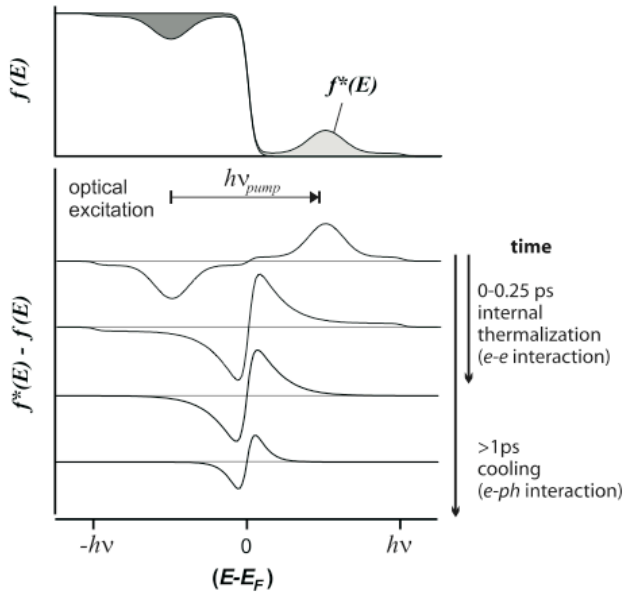

Figure 3.5 Schematic illustration of the non-equilibrium carrier distribution induced by absorbing femtosecond laser pulses of 790 nm wavelength. At first, 200 fs electron-electron scattering takes place, which redistributes the energy of the excited electrons. In turn, the energy is transferred to the lattice through electron-phonon interaction in a picosecond timescale. The above plot is adopted from [16].

In general the non-equilibrium carrier's distribution can be described by the Boltzmann equation:

$$\frac{\partial f^*}{\partial t} = \left(\frac{\partial f^*}{\partial t}\right)_{e-e} + \left(\frac{\partial f^*}{\partial t}\right)_{e-ph} \tag{3.3}$$

The collision term $\partial f^* / \partial t$ is zero for equilibrium distribution. The two terms on the right side of equation (3.3) represent the collision terms due to e-e and e-ph interactions, respectively. The non-equilibrium electron distribution is generated by absorption of energy from the pump pulse. Then the thermal equilibrium is acquired through a number of processes such as carrier-carrier, carrier-phonon scattering, electron-hole recombination and carrier diffusion out of the laser-excited area.

The carrier-carrier scattering takes place on the timescale of few hundredths of a femtosecond. This process changes neither the total energy stored in the carriers nor the carrier density, but it spreads out the non-equilibrium population in **k** space for electron densities greater than 10^{18} cm^3. Carrier-carrier interactions include e-e, hole-hole, and electron-hole scattering as well, which are separate processes. The first two interactions lead to internal thermalization of the excited electron and hole population while the third process leads to equilibrium of the conduction electron population with the hole population in the valence band. Inelastic scattering of carriers by phonons reduces the energy of the carriers, resulting in heating of the lattice. [21,22]. Assuming that the internal thermalization has taken place (i.e., ~200 fs after the excitation), the photoexcited carriers are still far out of equilibrium with the lattice on this timescale. The carrier-phonon scattering time is longer when compared to the carrier-carrier scattering time, due to the weaker coupling of the former.

In the experiments presented in the second part of this thesis we measure the phonon dynamics (see below Figure 4.2). The rise-time of the anti-Stokes Raman intensity, indicates that the scattering-time between electrons and phonons is on the order of ~400 fs, i.e., longer than the for e-e interaction. However, the phonons, which are primarily responsible for cooling the hot electrons, have energies on the order of meV, which is generally smaller when compared to the excess energy of the carriers. For instance, a carrier pair generated in a carbon nanotube with band gap ~1 eV (semiconducting) with photon energy at 1.6 eV has an excess energy of 600

meV, whereas the longitudinal optical (LO) phonon is 200 meV. Three phonons must be emitted in order for the carrier pair to get rid of its excess energy, or in other words 3 phonons must be emitted per electron excess energy measured form the bottom of the conduction band. The relaxation time due to LO emission is in the scale of picoseconds, around 1.2 ps at room temperature. More details about this process are presented in the Chapter 4.

Intervalley phonon scattering can also be present during the relaxation of the excited carriers [23]. Since the valleys are centered at different values of the crystal momentum, in order for the momentum to be conserved phonons with large wavevectors **q** are required. If the electron energy is lower than a phonon quantum below the minimum of the destination valley, then the intervalley scattering does not occur. The internal thermalizaton, which is in the scale of femtoseconds, and the e–ph interactions, which take place in the scale of picoseconds, are sufficiently different and thus easy to identify. Zamkov *et al.* [72] did measure the decay time of the excited charge carriers using MWNTs, and they found ~220 fs for the e-e interaction and 1.9 ps for the decay through e-ph interactions. These measurements are presented in Figure 3.6 and were taken with the same apparatus shown in Figure 3.2. Figure 3.6 shows the evolution of the photoelectron intensity versus the time as measured by Zamkov *et al*. [72]. The signal at longer time delays slowly decays and reflects the relaxation of the energy (temperature) of the thermalized electron population towards the lattice background value.

The electron-hole pairs can also recombine by radiative or non-radiative processes. During the first process a photon is emitted with energy equal to the energy difference between the initial and final states. Both the electron and the hole have identical wavevectors such that the energy and momentum conditions are conserved. The radiative process takes place on a nanosecond scale, therefore it is very slow compared to the other. Consequently, it does not play a significant role in the dynamics on the picosecond and sub-picosecond timescales. For the non-radiative processes, the so-called Auger recombination, the e-h recombination energy is not emitted as a photon but is transferred to an electron or a hole. While electron-hole energy transfer does not change the total energy of the e-h pair, Auger recombination leads to heating of the electronic system, which in turn can slow down the carrier dynamics. In carbon nanotubes, which are characterized as one-dimensional systems (1D), the effective Coulomb interaction is greatly enhanced and the optical transitions lead to the formation of strongly bound e-h pairs, known as excitons. Exciton-exciton annihilation through Auger recombination can be driven by

the Coulomb interaction if more than one exciton are present. It has been found that the rate of this process increases sharply with the exciton binding energy [11].

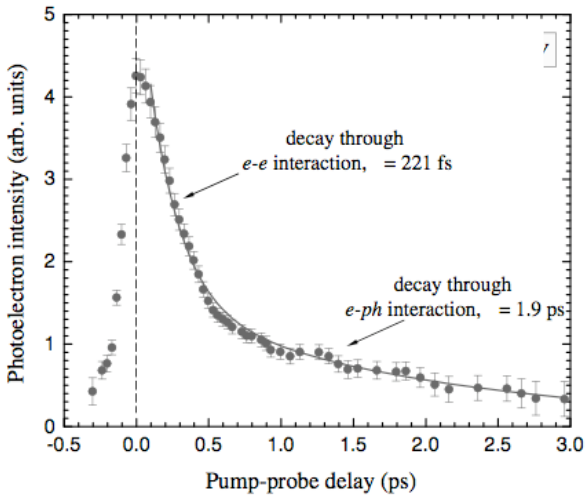

Figure 3.6 The two-photon photoemission signal as a function of the delay between the pump and the probe beams. The signal is recorded for electron energy of 170 ± 20 meV above the Fermi level. This figure is adopted from [72].

Another important mechanism that reduces the free-carrier density in the laser excited region is the diffusion, which refers to the average motion of free carriers from high-carrier density regions to low-carrier density regions. If the laser spot is larger than the penetration depth δ, then the carrier density varies only in the direction normal to the sample surface: $N(z) = N(0)exp(-z/\delta)$. In this case the diffusion time τ_{diff} is proportional to δ^2.

3.2.5 Excitation scheme and spectral analysis

The sample is initially excited with the IR pump beam with photon energy of 1.57 eV, which promotes the electron population from just below the Fermi level into the conduction band. The resulting charge distribution consisting of electron-hole pairs is then probed with the

delayed UV pulse, with an energy of 4.71 eV, which energetically exceeds the sample work function $e\Phi$ of ~ 4.41 eV by ~ 0.3 eV. In this configuration, the energy-dependent lifetimes of both the conduction electrons and the valence holes can be investigated [24]. The initial-state energy $(E\text{-}E_F)$ of photoemitted electrons with respect to the Fermi level, E_F, is obtained from their kinetic energy E_{kin} using the relation

$$(E\text{-}E_F) = E_{kin} + e\Phi - h\nu_{probe} \tag{3.4}$$

where $e\Phi$ is the work function of the sample and $h\nu$ the energy of the probe beam (UV at 263 nm).

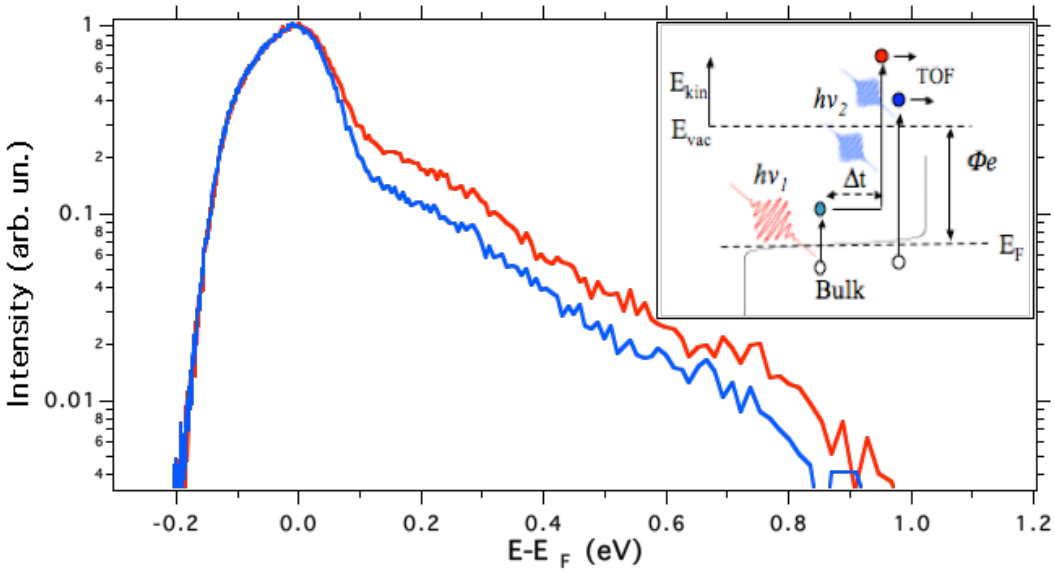

Figure 3.7 Photoelectron spectra of DWNTs. The red line is due to simultaneous pump and probe (790 nm and 263 nm) pulses, while the blue line is only due to probe pulse (only 263 nm). The inset represents the excitation scheme (more details are given in the text).

The photoelectron signal before and after the perturbation with the pump pulse is presented in Figure 3.7. The probe beam exceeds the work function of the sample, thus it can

excite electrons from below the Fermi level to the vacuum in our experiment. In order to isolate the photoelectrons originating from the excited states above the Fermi energy, we recorded the change in the photoemission signal induced by the IR pump pulse ($\Delta I = I_{pump+probe} - I_{probe}$). The spectrum due to probe beam only has been subtracted from the spectrum due to both beams.

Figures 3.8 and 3.9 present the difference between the two spectra. This ‘‘excitation’’ difference reflects the non-equilibrium carrier distribution as induced by the pump pulse. The negative signal below the Fermi energy is due to vacancies induced by the pump pulse. In contrast, the positive signal above the Fermi level increases due to the electrons that have been removed from occupied states.

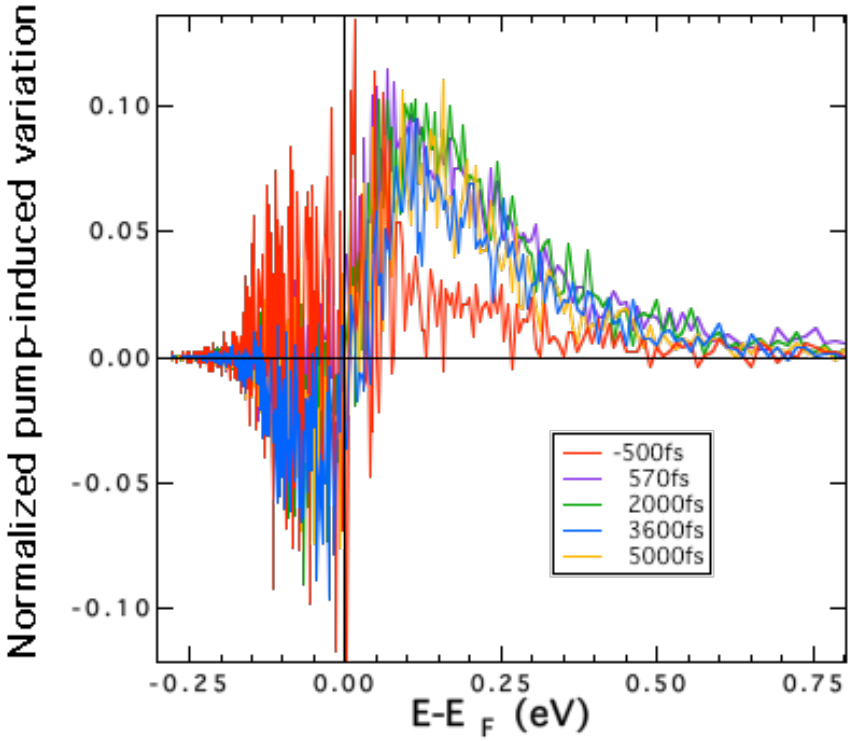

Figure 3.8 The time evolution of the photoexcitation spectra, which show the changes in the electron distribution due to absorbed energy from the IR pump pulse. For negative delay (red line) the signal is very small and is due to the UV probe pulse, which exceeds the work function of the sample in energy.

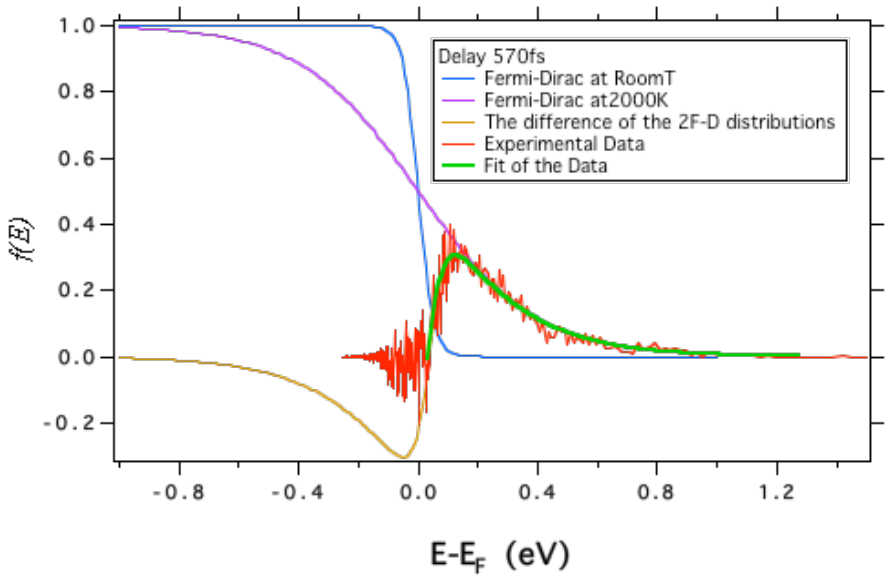

Figure 3.9 Changes in the Fermi-Dirac distribution due to different electronic temperatures. The red line shows the experimental data for delay 570 fs. The brown line is the difference of two Fermi-Dirac (F-D) distributions; one of them characterized by the room temperature 300 K and the other one by an elevated temperature of 2000 K.

A fit to the Fermi-Dirac (F-D) distribution of the experimental data is usually used to determine the electronic-system temperature, and in turn estimate the internal energy. The function which has been used for this purpose is the difference between $f(T_e)$, which represents the pump-induced changes in the distribution of the electrons with T_e being the electronic temperature, and the distribution $f(T_l)$, where T_l is the lattice temperature. This is a very good approximation for estimating the internal energy of a non-thermal electronic system [16]. For long delays (i.e. > 400 fs) between the pump and probe pulse, an equilibrium between electrons and phonons has been established and the F-D statistic describes the system. Figure 3.10 shows the fit of the data with the F-D distribution for a delay of 570 fs. The data are well described at this delay time. The reason is that the system requires some finite time, a few hundreds of a

femtosecond, in order to reach its internal equilibrium after the perturbation by the pump pulse, which can then be described by a F-D statistics.

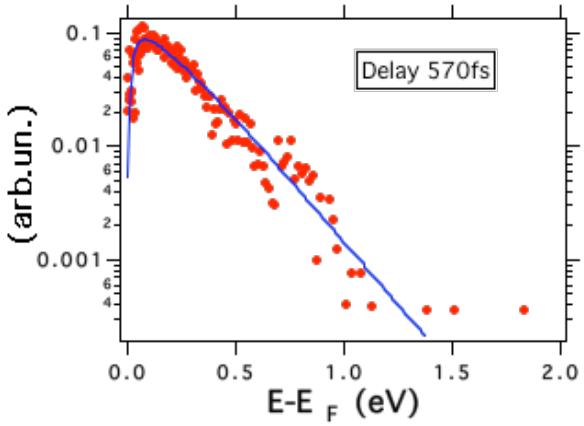

Figure 3.10 Photoexcitation spectra for a delay (570 fs) between the pump and the probe beams. The data are well described by the Fermi-Dirac statistics at an elevated temperature T_e, of the electron gas.

Another way of calculating the internal energy of the excited electronic gas is by using equation (3.13). It is described in the next section.

3.3 Two-Temperature model approximation, internal thermalization cooling of the electron gas and electron-phonon interactions

The optically excited carriers, electrons in the conduction band and holes in the valence band, lose their excess energy and relax to the band minimum (electrons) or to the band maximum (holes) by several types of interactions as has been mentioned above. The cooling of the thermalized electron gas with temperature T_e can be attributed to the coupling with the phonons of the lattice with temperature T_l. The Two-Temperature model (TTM) [25], which is

described by a set of coupled differential equations (3.7 and 3.8), is invoked to give a description and interpretation of the electron-phonon coupling between the carriers' and the phonons' dynamics.

3.3.1 Internal thermalization

The electron gas immediately after the excitation is internally thermalized mostly through electron-electron scattering. At high excitation energies above the Fermi level, E_F, the relaxation rate of the hot electrons is faster since more phase space is available. At energies close to the Fermi level this process becomes slower due to the secondary electron contribution. The FLT for electron interactions explains this trend. The lifetime $\tau_{e\text{-}e}$ is given by equation

$$\tau_{e-e} = \tau_0 \left[\frac{E_F}{E - E_F} \right]^2 \quad \text{with} \quad \tau_0 = \frac{64}{\pi^2 \sqrt{3\pi}} \sqrt{\frac{m}{ne^2}} \tag{3.5}$$

where m and e are the electron mass and charge, respectively, and n is the density of the electron gas [18,19]. A behavior similar to lifetime behavior described by equation (3.5), is observed by Zamkov *et al*. [17]. They performed measurements close to the Fermi level ($0 < E - E_F < 170$ meV) and found that the measured lifetimes follow the FLT power-law energy dependence [17]. The decay rates depend not only on the carrier energy, but also on the initial-state sub-band, due to constrains imposed on e-e scattering processes by momentum and energy conservation [16,26].

The decay of the primary electron distribution is described by the differential equation,

$$\frac{dN(E,t)}{dt} = S(t) - \frac{N(E,t)}{\tau_{e-e}(E - E_F)} \tag{3.6}$$

where $S(t)$ is the excitation rate that is proportional to the pump pulse envelope, and $N = N(E,t)$ is the transient population.

3.3.2 Electron phonon interactions

The thermalized electron gas due to e-e interactions even though it has acquired internal equilibrium (redistribution of the energy) is far away from equilibrium with the lattice. At this stage the electrons follow the F-D distribution with characteristic temperature T_e. This temperature represents the excess energy of the non-equilibrium electrons (initial free-carrier excess energy) and it corresponds to the energy above the conduction band minimum for electrons and the energy below the valence band maximum for the holes. The time evolution of the energy in the two subsystems is described by a set of coupled differential equations introduced by Anisimov *et al*. [25]

$$C_e\left(T_e\right)\frac{dT_e}{dt} = \nabla\left(\kappa\nabla T_e\right) - H\left(T_e,T_l\right) + S(t) \tag{3.7}$$

and

$$C_l\left(T_l\right)\frac{dT_l}{dt} = H\left(T_e,T_l\right) \tag{3.8}$$

In equation (3.7), C_e is the electronic heat capacity, and $\nabla\left(\kappa\nabla T_e\right)$ is the diffusive electronic heat transport out of the excited region. This term can be neglected because it describes a very slow process. For instance, it is ~ 0.05 W/cm·K for graphite. The diffusion timescale is of the order of 100 ps. This process is too slow to be relevant to the time scale of the observed electron-cooling rate. The coupling term $H\left(T_e,T_l\right)$ plays a crucial role and it represents the rate that the electronic system loses energy towards the lattice when $T_e > T_l$. In other words, it describes the rate that the energy flows from the electronic system to the phonons. $S(t)$ is the source term and it describes the absorbed laser energy density per unit time.

The lattice can be thought of as a sink which stores all the injected energy, a process which is completed on the picoseconds timescale. Regarding equation (3.8), C_l is the lattice heat capacity with $C_l \gg C_e$. The coupling term $H\left(T_e,T_l\right)$ is proportional to $T_e - T_l$. The diffusive

term $\nabla(\kappa\nabla T_l)$ is absent in this equation because heat diffusion occurs much more rapidly through the electron gas than through the lattice phonons. The electronic heat capacity is then given by [27]

$$C_e(T_e) = \gamma T_e \text{ with } \gamma = \frac{2}{3}\pi^2 N(E_F) k_B^2 T_e \tag{3.9}$$

where $N(E_F)$ is the density of states at the Fermi energy. For instance, in metallic SWNT (9,9) the density of states $N(E_F)$ at the Fermi level is 0.015 atom^{-1}eV^{-1} [16,26], while for the graphite the $N(E_F)$ is 5.5×10^{-3} atom^{-1}eV^{-1} [16,26]. Thus an average electronic heat capacity with a 1:2 mixture of metallic to semi-conducting tubes is 12 μJ/mole·K, which is almost the same as for the graphite 13.8 μJ/mole·K. The electronic heat capacity at room temperature is much smaller than the lattice specific heat, which is 7.8 J/mole·K [24]. Thus the lattice temperature does not increase noticeably.

Neglecting the lattice heat transport (since it occurs in the nanosecond scale), and assuming that the radius of the laser spot is much larger than the penetration length (~15 nm for graphite at 790 nm wavelength) and using the fact that the specific heat of the lattice is 100 times larger than the electronic specific heat, we end up with the simple formula

$$C_e(T_e)\frac{dT_e}{dt} = -H(T_e, T_l) \tag{3.10}$$

where $C_e(T_e) = \gamma T_e$. The energy transfer rate is a sum over all the elementary one-phonon absorption and emission processes weighted by the energy transfer per collision [28]

$$H(T_e, T_l) = \sum_{q,k} \hbar\omega_q (W_{q,k}^e - W_{q,k}^a) \tag{3.11}$$

where $W_{q,k}^e$ and $W_{q,k}^a$ are the transition rates for emission or absorption of a phonon - with wavevector q - by an electron in the state k. The set of the coupled differential equations (i.e., 3.7

and 3.8) is know as the Two Temperature Model (TTM) [25], which describes the energy flow rate after the laser excitation of the electronic system.

Experimentally, the energy transfer rate $H(T_e,T_l)$ can be measured using TR-TPP spectroscopy as follows. The function $H(T_e,T_l)$ can be written in terms of the internal energy U_{int} of the electronic system

$$H(T_e,T_l) = -\frac{dU_{int}}{dt} \tag{3.12}$$

The calculation of the internal energy U_{int} can be carried out using only the positive energies from the photoemission signal (such as the one shown in Figure 3.8).

$$U_{int} = U_{int}(T_l) + 2B\int_0^{\infty} dEE\Delta I(E + e\Phi - h\nu) \tag{3.13}$$

The first term $U_{int}(T_l)$ in equation (3.13) is the electronic energy before excitation when the system is in equilibrium with the lattice. The factor of 2 is due to the contribution of the holes and B is a normalization constant, while ΔI is the measured change in the photoemission signal. The constant B is calculated using the temperature obtained by the F-D differences fit (see Figure 3.9) but for very long delay times such that the internal thermalization is switched off.

We note that both methods, i.e., the F-D distributions difference and formula (3.13), give similar results with very small deviations.

The internal energy $U_{int}(T_e)$ of the electron gas is calculated using the relation $U_{int}(T_e) = \gamma T^2$ with γ = 2.4 J/m^{3}K^2 and T derived from the F-D fit. The decay curve of this energy as a function of time is presented in Figure 3.11. The experimental data have been fitted with a simple exponential decay function $exp(-t/\tau)$, and a decay time of 1.52 ± 0.76 ps has been found. Our data correspond to delays ≥ 500 fs, where in this region the e-e interactions have been switched off. The laser beam instability (vibrations, drifts) did not allow us to gather data for shorter delay times.

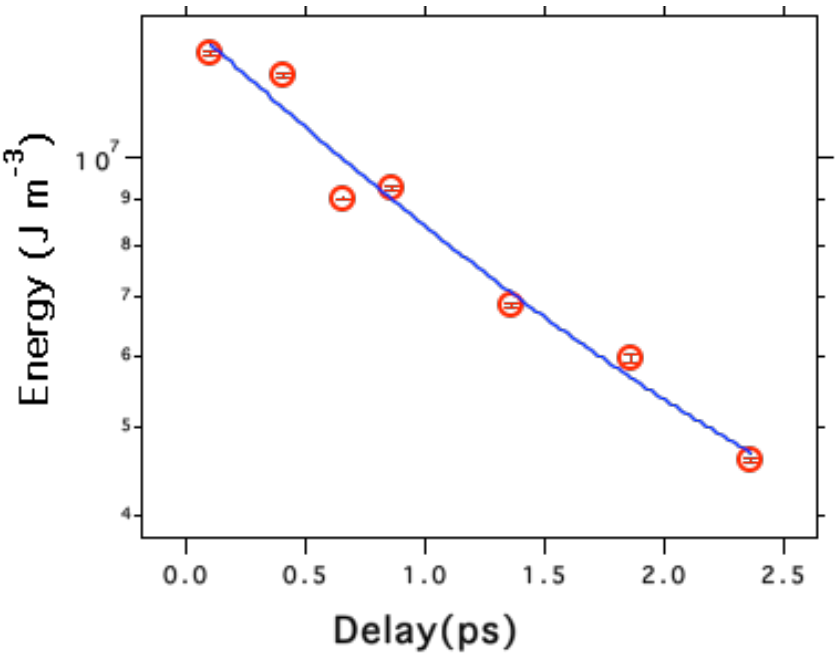

Figure 3.11 The temporal evolution of the energy density $U_{int}(T_e)$. The blue line is an exponential fit of the data.

The energy transfer rate $H(T_e,T_l)$ is obtained by differentiation of the data shown in Figure 3.11 with respect to time. These rates are plotted as a function of the temperature difference ΔT = (T_e - T_l), where T_l = 300 K, in Figure 3.12. A strong non-linear increase in the rate with the temperature is observed. Using the theory of Allen [14, 26], the data shown in this figure can be fit with

$$H(T_e,T_l) = h\frac{(T_e - T_l)^5}{T_e}, \tag{3.14}$$

where $h = \frac{144\zeta(5)k_B C_e}{\pi\hbar}\frac{\lambda}{\Theta_D^2}$, where $\zeta(5) = 1.0369$ is Riemann's zeta function, Θ_D is the Debye temperature (~1000 K), and λ is the mass-enhancement parameter [31-33], which is determined to be $\lambda = (1.16 \pm 0.16) \times 10^{-4}$.

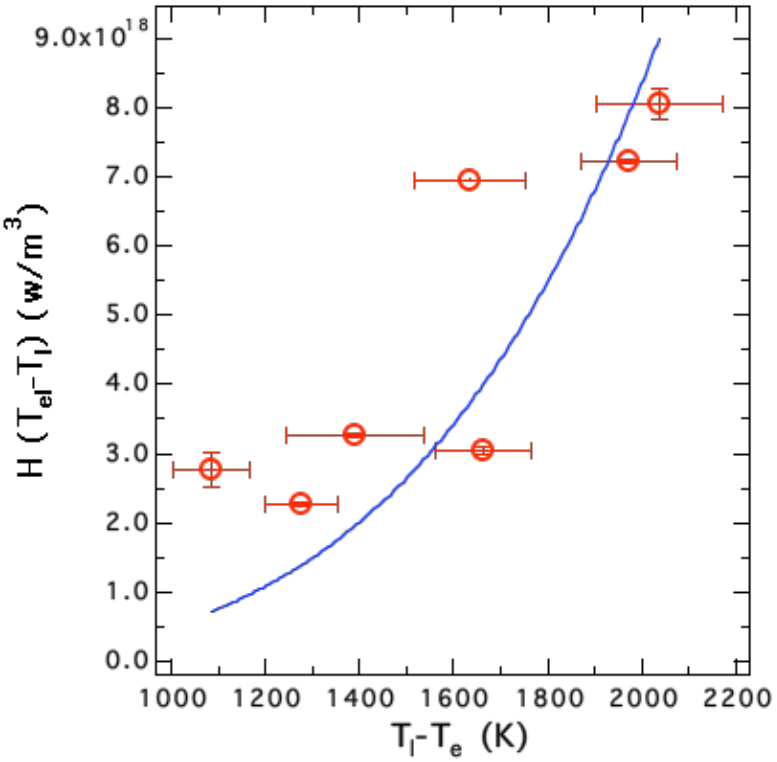

Figure 3.12 The energy transfer rate, $H(T_l\text{-}T_e)$, from the electronic system to the lattice versus the temperature difference between the electronic system and the lattice. The solid line is the fit of the data given by equation (3.14), with h as adjustable parameter.

Using the following equation

$$\frac{1}{\tau_{\text{e-ph}}} = 24\pi\zeta(3)\frac{\lambda}{1+\lambda}\left(\frac{T_e}{\Theta_D}\right)^3 \omega_D \qquad (3.15)$$

given by the Allen theory [14,31] and the value of the mass enhancement parameter, λ, which we found above, it is possible to calculate the electron-phonon scattering time. In the above equation $\zeta(3) = 1.2020$ and $\omega_D \sim 2.3 \times 10^{13}$ sec^{-1} is the Debye frequency, while using $\lambda = (1.16 \pm 0.16) \times 10^{-4}$ gives $\tau_{e\text{-}ph} = 25 \pm 1$ ps which, in combination with the Fermi velocity of $\upsilon_F = 10^6$ m/sec, corresponds to 25 ± 1 μm mean free path $l_{e\text{-}ph}$ at room temperature for DWNTs. Hertel *et al.* [15,16] have calculated the same order of magnitude for the mean free path of SWNTs in bundles. Actually they found it equal to 15 μm. Taking into account that in our study the samples are DWNTs and the fact that the resistivity is inversely proportional to the number of shells, this large value of the $l_{e\text{-}ph}$ is totally compatible with previous studies.

To conclude this section, we studied the energy transfer rate from the electronic system to the lattice, and we determined the mass-enhancement parameter $\lambda = (1.16 \pm 0.16) \times 10^{-4}$, which represents the electron phonon coupling strength. Using this information we finally found the mean free path for DWNTs samples to be $l_{e\text{-}ph} = 25 \pm 1$ μm, which is of the same order of magnitude as the values found previously for SWNT.

CHAPTER 4 - Temperature dependence of the anharmonic decay of optical phonons in carbon nanotubes and graphite

4.1 Introduction

Carbon nanotubes, due to their structure, have unique properties and are ideal systems for the study of many fundamental physical phenomena in one-dimensional materials. Lately, graphite has also attracted great interest because of its similarity to graphene and nanotubes. In particular, SWNTs are potential candidates for nanoscale electronic devices and interconnects, based on the fact that they can carry a high current density. However, there are mechanisms that limit the current through the nanotubes, such as electron-electron or electron-phonon scattering. Extensive investigations of electron-electron [34-36] and electron-phonon [37-39] interactions have been reported in the literature. The phonon-phonon interactions, which are related to the temperature, play an essential role in thermal transport and induce variations in the mobility of the charge carriers. A non-equilibrium population of optical phonons can be created at the zone-center and at the edges of the Brillouin zone, for SWNTs under high electrical bias conditions, [29,40-43] or by optical excitation. The presence of these hot optical phonons has been shown to reduce the mobility of the charge carriers. Current saturation and negative differential resistance behavior in nanotubes have been attributed to these hot phonons [29,42-44]. It is apparent that the decay rate of these phonons, through anharmonic interactions, will influence the non-equilibrium phonon populations and, hence, the electrical transport properties. Raman scattering provides a means of study of such nonequilibrium phonons. Important information about the mechanisms responsible for the broadening can be extracted from the linewidth of the Raman signal [45,46]. Temperature-dependent effects including phonon-phonon and electron-phonon scattering contribute to the total linewidth. However, the dominant contribution to the linewidth results from the electron-phonon interaction; thus it makes it difficult to deduce the lifetime of the hot phonons against anharmonic decay from Raman line-broadening measurements.

An alternative method is to probe the lifetime of the non-equilibrium optical phonons directly in the time domain [47]. This can be accomplished by time-resolved Anti-Stokes Raman

(ASR) scattering. This technique constitutes a reliable tool for investigating these non-equilibrium populations. Measurements of the lifetime of the zone-center (G-mode) optical phonons in graphite and SWNT in room temperature have already been carried out by our group [48,59], by monitoring the ASR signal in the time domain. Decay times of 1.1 ± 0.2 ps (for SWNTs) and 2.2 ± 0.1 ps (for graphite) were found. Recently Kang *et al.* [49] extended the above work for SWNTs from room temperature to ~ 450 K and found a decay time ranging from 1.2 ps to 0.9 ps.

In the present work we measure by time-resolved anti-Stokes Raman spectroscopy (ASR) the relaxation rate of optically excited zone-center (G-mode) optical phonons over an extended temperature range, i.e., 6 K to 515 K for SWNTs and from 340 K to 685 K for graphite. Using these data, we examine possible relaxation channels of the zone-center optical phonons. The phonon population $n(\omega,T)$ is a function of the temperature T and therefore, by changing this variable, we can infer what routes the energy follows in order to relax through the anharmonic interactions. It is known that an increase of the temperature increases the density of the excited acoustic phonons. Therefore, the collision probability between the optical and acoustic phonons increases, resulting in an increased relaxation rate. The frequency of the optical phonons is also slightly shifted [50-53,60].

4.2 Experimental

4.2.1 Laser system and pump-probe setup for time-resolved Raman spectroscopy

In our experiment the laser beam exciting the samples had an 800 nm central wavelength, and it was supplied by a 1-KHz repetition rate, regeneratively-amplified, mode-locked Ti:Sapphire laser, with pulse duration of ~100 fs. To probe the samples, we introduced a second beam at 400 nm at an adjustable delay time. The probe beam, obtained by frequency doubling the 800 nm pump beam, had a duration of ~150 fs. The beams had parallel linear polarization. The fluences were 0.7 mJ/cm^2 for the probe and 2 mJ/cm^2 for the pump (see Figure 4.1). The samples were mounted on the cold finger of a cryostat (model RC102 from CIA) with optical

access. All measurements were made under vacuum (10^{-6} Torr). Liquid helium was used to cool the samples for the low temperatures (6 K and 100 K) regime. For the high temperatures, a homemade electrical heater was used. All temperatures were measured with a type K thermocouple.

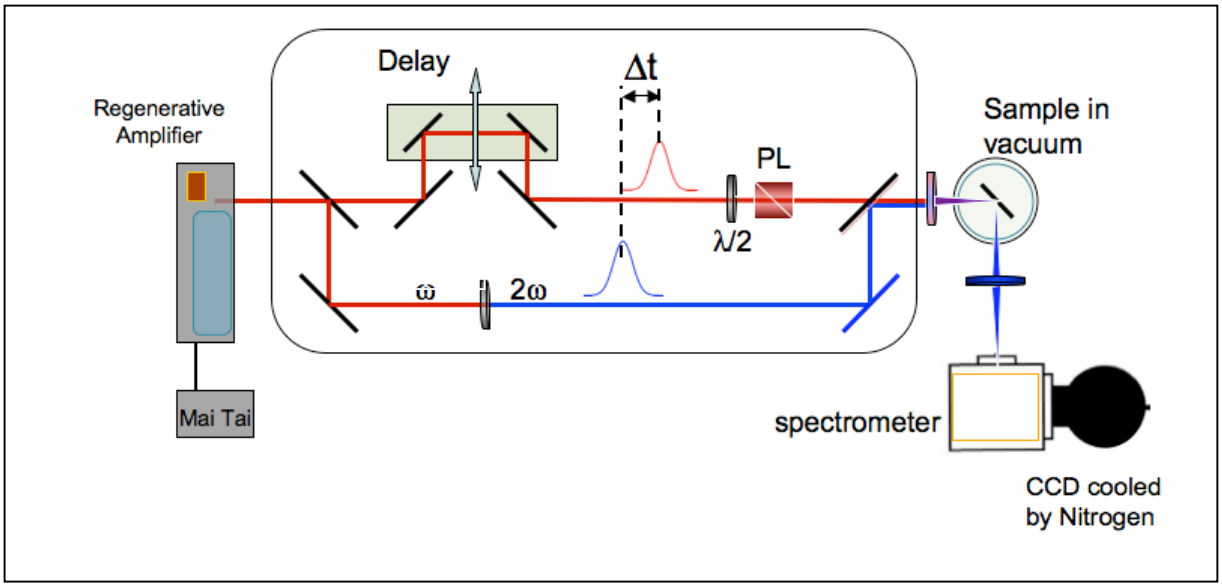

Figure 4.1 Schematic representation of the experimental setup. The delay Δt between the pump and the probe pulses was introduced by a mechanical delay stage. The scattered Raman radiation produced by the probe beam was collected as shown and analyzed with a spectrometer.

A charge-coupled device (CCD) cooled by liquid nitrogen was used to detect the scattered light, which was first collected through a laser blocking bandpass filter and dispersed by a single-pass spectrometer equipped with a diffractive element of 1800 lines/mm. The resolution of our system was restricted by the bandwidth of the probe pulses.

All our samples were obtained from commercial sources. The SWNTs were synthesized by the High Pressure Carbon Monoxide (HiPCO) process, producing nanotubes with 1-2 nm diameter, 5-30 μm length, and purity better than 90%. The SWNTs were a mix of

semiconducting and metallic species. Initially, they were in powder form and were dissolved in dichloroethane, in order to deposit them on a quartz substrate. For the graphite sample, we used Highly Oriented Pyrolitic Graphite (HOPG) with a mosaic spread of 0.8°. Our samples were commercial and in particular SWNTs purchased from Cheap Nanotubes Companies and graphite from Advanced Ceramics.

4.2.2 Results and discussion of time-resolved anti-Stokes Raman scattering

The pump beam induces a non-equilibrium optical phonon population. This quantity is then monitored by the strength of the ASR signal, which is directly proportional to the population of excited phonons ($I \propto n$) (see Figure 4.2).

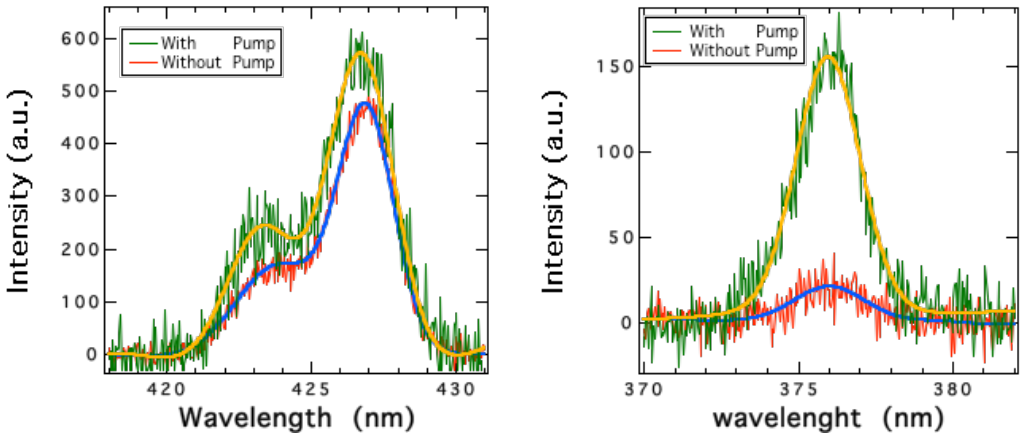

Figure 4.2 Raman spectra of the G-mode for the Stokes and antiStokes signal, with and without pump excitation. The probe wavelength for the Raman measurements is 400 nm. The left panel shows the Stokes signal at 427 nm, with and without excitation of the pump pulse. The shoulder at 423 nm is the D-mode peak due to defects in the sample. The right panel shows the anti-Stokes Raman signal at 375 nm, with and without excitation. It is obvious that the effect of the excitation pulse is more pronounced. A slight blue shift is observed for the pumped spectra of Stokes and anti-Stokes in both panels (see details in the text).

Thus, by introducing a time delay between the pump and the probe beam, we can monitor directly in the time domain the decay of the phonon population. The procedure we followed was to collect spectra as a function of the delay time and integrate the Raman intensity measured at each delay.

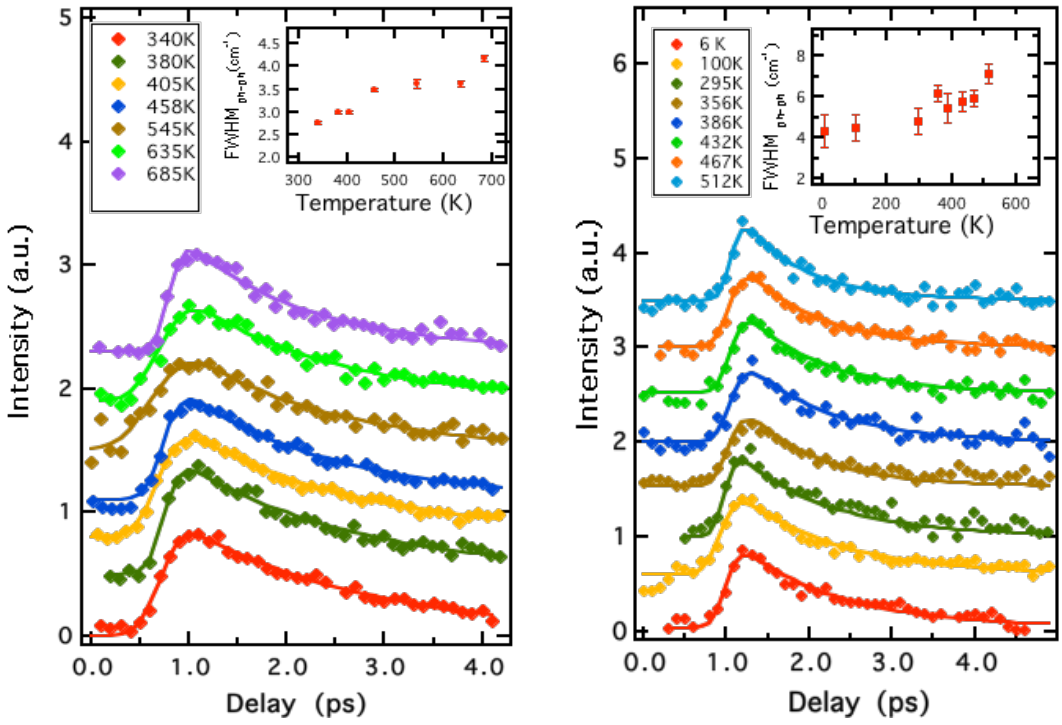

Figure 4.3 Anti-Stokes Raman signal for graphite (left panel) and for SWNT (right panel). The signal of the E_g mode optical phonons is plotted as a function of the delay time Δt introduced between the pump beam (800 nm) and the probe (400 nm) beams, for different initial sample temperatures. The data are fitted with an exponential decay, convolved with the instrumental response function (shown as solid lines). The inset in each plot shows the contribution $\Gamma_{ph\text{-}ph}$ to the Raman line (in cm^{-1}) due to phonon-phonon interactions. The $\Gamma_{ph\text{-}ph}$ is a small contribution to the total width and is given by the imaginary part of the phonon self energy.

We derive the decay time τ by fitting the data with the convolution of the instrument response function and an exponential decay. Figure 4.3 displays our measurements of the anti-Stokes

Raman scattering intensities for graphite and SWNTs as a function of the delay of the probe beam for different temperatures *T*. We also show the corresponding decay rate (FWHM of spectral line in cm^{-1}) in the inset of each set of measurements.

In terms of phonon lifetimes, we measured 1.23 ± 0.15 ps at 6 K and 0.75 ± 0.15 ps at 515 K decay times for SWNTs, corresponding to our extreme temperature limits. For graphite we found 1.92 ± 0.02 ps at 340 K and 1.27 ± 0.05 ps at 685 K. Our measurements for room temperature are consistent with results from previous studies [48,49,59] for both samples. Measurements at 6 K and 100 K for SWNTs, i.e., 1.23 ± 0.15 ps and 1.18 ± 0.08 ps, respectively, show no significant difference.We find that the relaxation time of the zone-center optical phonons (G-mode) in the nanotubes is shorter compared to that in the graphite. This result is probably due to the coupling between the G-mode and the additional radial-breathing mode (RBM) [54], pinch, and bending modes that do not exist in the graphite.

4.2.3 Anharmonic scattering

We first consider briefly the origin of the non-equilibrium phonons produced by the laser pump pulse. These phonons are produced by two mechanisms: by absorption of a photon [37,39] or by exciton-exciton annihilation [55] (Auger recombination). The latter procedure produces a high-energy electron-hole pair that is cooled by emission of phonons. The cooling process described above will lead to a large non-equilibrium population of optical phonons and also to an electron-hole gas, whose temperature is higher than that of the lattice. The fast rise time of the ASR signal verifies that the electron-phonon interaction is also a very fast process. According to our measurements (Figure 4.3) the rise-time for the build up of the phonon population is < 400 fs for both samples.

From the ratio of anti-Stokes to Stokes intensities I_{AS}/I_S at 300 K (Figure 4.2), we obtain a G-mode phonon population n = 0.3 due to the optical excitation for SWNT. From this we deduce an effective temperature of 1560 K for the G-mode phonons, which confirms the creation of this non-equilibrium distribution by the pump pulse. The temperature is much greater than what could be caused by laser heating effects. We can estimate an upper limit of the local surface temperature of the graphite under the laser irradiation. The fluence we use is ~2 mJ/cm^2 and the

radius of the spot is ≥ 500 μm. The penetration depth is ~ 15 nm [56] at 800 nm and C_p = 8.58 J/mol·K at 300 K. The transient temperature increase of the sample surface after the pumping is $T = F(1\text{-}R)\alpha/\rho C_p \sim 450$ K, where the reflectance R is equal 50% [57]. The considerably higher effective temperature observed for the G-mode optical phonons shows that the pump pulses create non-equilibrium phonon populations.

We now discuss the temperature dependence of the decay processes for the G-mode phonons. In the harmonic approximation, phonons are independent of each other. However, in a real crystal, the vibrations are not harmonic and the V_3 (third) anharmonic term of the expanded potential energy of the crystal describes the phonon-phonon interactions. These become more important as the temperature of the crystal increases.

We can write the intrinsic linewidth as $\Gamma_{in} = \Gamma_{e\text{-}ph} + \Gamma_{ph\text{-}ph}$, where $\Gamma_{ph\text{-}ph}$ represents the inverse of the anharmonic phonon lifetime, $1/\tau$, and $\Gamma_{\text{e-ph}}$ is the contribution from electron-phonon interactions. The width $\Gamma_{ph\text{-}ph}$ due to phonon-phonon interactions is given [50-53,60] by the imaginary part of the self-energy of the phonons

$$\Gamma_{ph-ph}(\mathbf{q}', j, \Omega_G) = \frac{36\pi}{\hbar^2} \sum_{q, j_1, j_2} \left| V_3 \begin{pmatrix} \mathbf{q}' & \mathbf{q} & -\mathbf{q} \\ j & j_1 & j_2 \end{pmatrix} \right|^2 \{[1 + n(\mathbf{q}, j_1) + n(-\mathbf{q}, j_2)] \times \delta(\Omega_G(\mathbf{q}') - \omega(\mathbf{q}, j_1) - \omega(-\mathbf{q}, j_2)) + 2[n(\mathbf{q}, j_1) - n(-\mathbf{q}, j_2)] \times \delta(\Omega_G(\mathbf{q}') + \omega(\mathbf{q}, j_1) - \omega(-\mathbf{q}, j_2))\} \quad (4.1)$$

where $n = [1/\exp(\hbar\omega_{\mathbf{q},j}/k_BT)\text{-}1]^{-1}$ is the Bose-Einstein distribution. The frequencies $\omega(\mathbf{q}, j_1)$ and $\omega(-\mathbf{q}, j_2)$ are those of the lower energy phonons into which the G-mode phonon (at frequency Ω_G) decays. Here j_1, j_2 denote different branches in the phonon dispersion curves. The matrix element V_3 is proportional to the third derivative of the inter-atomic displacement. At the Γ point of the Brillouin zone the optical phonons are defined to have zero wave vectors ($q' = 0$). Since conservation of energy and momentum must be satisfied, we require $\Omega_G(\mathbf{q}') = \omega(\mathbf{q}, j_1) + \omega(-\mathbf{q}, j_2)$ with $\mathbf{q}' = \mathbf{q}_{j_1} - \mathbf{q}_{j_2}$. The first term in equation (4.1) corresponds to

the down-conversion process, where the initial Ω_G phonon with wave vector $q' \sim 0$ decays into two lower-energy phonons $\omega(\mathbf{q}, j_1)$, $\omega(-\mathbf{q}, j_2)$ with opposite wave vectors (Figure 4.4). The down-conversion process always has a finite contribution even at 0 K. The second term describes the up-conversion process, where an optical phonon is scattered by a thermal phonon of frequency $\omega(\mathbf{q}, j_1)$, resulting in a phonon of higher frequency $\omega(\mathbf{q}, j_2)$, This process is unimportant in CNTs and graphite, since the zone center optical phonons have (essentially) the highest frequency of any phonons in the system. Thus the second term is not included in the function used to fit our data shown in Figure 4.5.

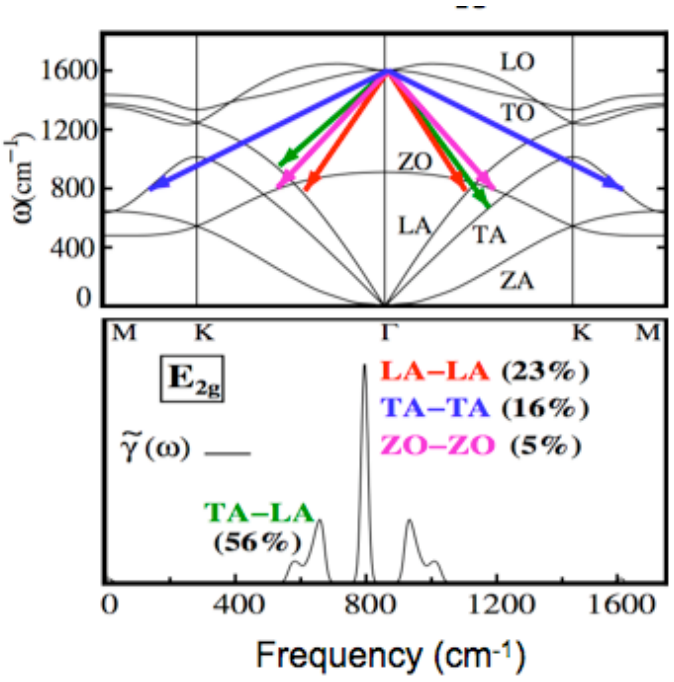

Figure 4.4 The upper panel represents the decay channels of the G-mode optical phonons at the Γ point of the Brillouin zone that have been predicted theoretically. The lower panel shows the predicted spectrum of the generated phonons. These plots have been adapted from [61].

Another implication of equation (4.1) is that the linewidth depends on the temperature through the occupation numbers, n, of the phonons, into which the optical phonons decay. Analysis of the

temperature dependence of the phonon lifetime thus provides information about possible channels. For $j_1 \neq j_2$, equation (4.1) results in a combination channel; for $j_1 = j_2$ (Klemens model [58]), it gives an overtone channel, depending on the band structure of the material under investigation.

In the Klemens model [58], an optical phonon decays into two acoustic phonons of opposite wave vectors, **q**, and equal energy $\omega(\mathbf{q},j_1) = \omega(-\mathbf{q},j_2)$ (overtone). This leads to $\Gamma_{ph\text{-}ph} \propto [1+2n(\Omega_G/2)]$. However, the last relation does not fit our data well, suggesting the overtone channel is less likely in our case than the combination channels. Therefore we fit our data with equation (4.1) for a decay into pairs of phonons with different energies. We thus treat ω_1 as an adjustable parameter, with the sum of the two phonons giving Ω_G = 1585 cm^{-1}. Figure 4.5 represents a comparison of the temperature dependence of the experimental data and the results of the fit to equation (4.1). We find 306 cm^{-1} and 1279 cm^{-1} for the frequencies of the resulting phonons and 0.82 ± 0.05 ps^{-1} for the rate $\Gamma_{ph\text{-}ph}$ at T = 0 K in SWNTs (see Figure 4.5). For graphite, the corresponding parameters are 452 cm^{-1}, and 1133 cm^{-1} with an anharmonic rate equal to 0.47 ± 0.05 ps^{-1} at zero temperature. These results are summarized in Table 4.1.

Sample	$\omega(\mathbf{q},j_1)$ [cm^{-1}]	$\omega(-\mathbf{q},j_2)$ [cm^{-1}]	Anharm. const. [ps^{-1}]
Graphite	452	1133	0.47 ± 0.05
SWNT	306	1279	0.82 ± 0.05

Table 4.1 Frequencies of the decay channels of the G-mode phonons for graphite and SWNTs. These values arise from the fits of equation (4.1), as discussed in the text.

The occupation of the created phonons should follow the selection rules, L⇔T+T, L⇔T+L [57,62], where T and L denote the transverse and longitudinal polarization branches, respectively. We find that the values of ω_1, and ω_2 for the graphite are in good agreement with

the theoretical prediction of Bonini *et al.* [61]. Since there is no theoretical prediction for SWNT, we compare our results with that of graphene [61].

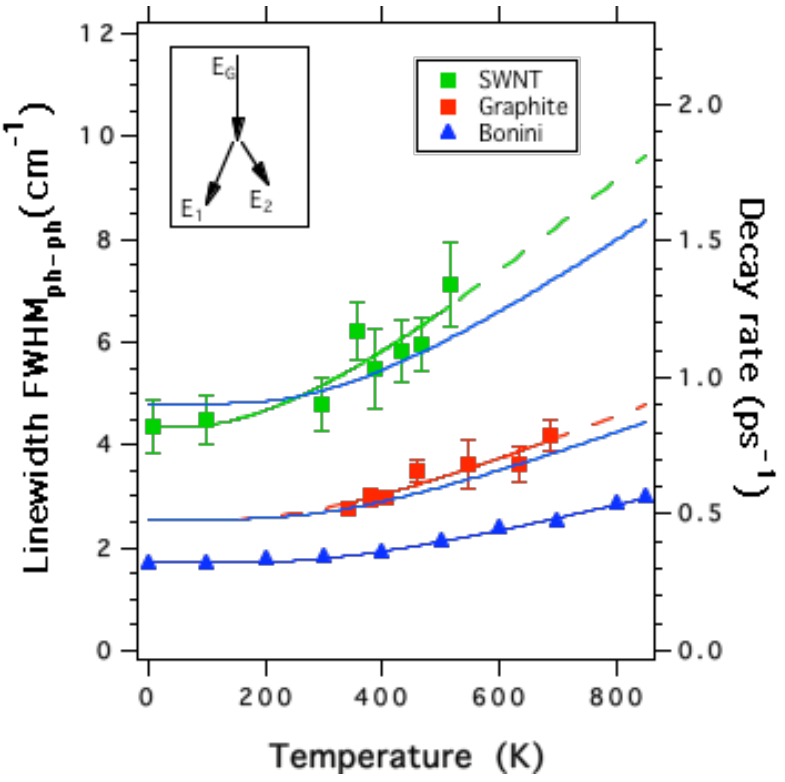

Figure 4.5 The relaxation rate of the G-mode optical phonons in SWNT and graphite as a function of temperature. The left vertical axis represents the corresponding width (measured as the FWHM) of phonon-phonon interactions in cm^{-1}, while the right vertical axis gives the decay rate in ps^{-1}. The data for SWNT (green points) and graphite (red points) are fitted with equation (4.1) (solid lines), while the extrapolations of these fits are shown with dashed lines. The blue points represent the theoretical prediction of Bonini [61] for the decay rate of graphite (see text). Since there is no prediction for SWNT, we compare our results with the predictions of [61] for the graphene/graphite. In particular, the two top blue curves are the theoretical models of [61] multiplied by factors of 1.5 and 2.8, respectively. However, one has to keep in mind that two somewhat different systems have been compared. The inset shows a three-phonon process, where the Ω_G decays into two lower energy phonons $E_1 = \hbar\omega(\mathbf{q}, j_1)$ and $E_2 = \hbar\omega(-\mathbf{q}, j_2)$.

We find that the relaxation rate for SWNTs while of the same order of magnitude as for graphene, is approximately a factor of two greater. This is presumably due to the presence of additional phonon modes, as mentioned above. From our analysis above, the inferred energies of the two final phonons are between ~ 300 cm^{-1} and $\sim$1280 cm^{-1}.

Bonini *et al*. performed *ab-initio* calculations of the anharmonic decay of the G-mode phonons in graphene. They found that the higher percentage (56%) follows the decay channels TA-LA and the remaining (44%) follows all other channels. We can safely argue that the decay channels that we found in the energy range mentioned above are the TA, LA branches. The difference between ω_1 and ω_2 is 973 cm^{-1} for SWNT, and 681 cm^{-1} for graphite.

In the high-temperature regime, i.e., for $T \gg \Theta_D$, where Θ_D is the Debye temperature, $n(\omega) \approx \hbar\omega / k_B T$. Thus, it can be shown from equation (4.1) that $1/\tau \propto T$. For the G-mode optical phonons equal to 0.196 eV (corresponding to a temperature of $\sim$ 2279 K) a very high temperature must be reached before the relaxation rate becomes linear with the temperature. This also means that for other modes with lower energy the linear behavior will be reached at lower temperatures. According to our results (Figure 4.5), the linear behavior of the relaxation rate is observed at $T \geq 295$ K, so it cannot be considered that we are in the high-temperature limit. This has also been observed by Kang *et al.* [49] without any explanation.

All the measured decay lifetimes for SWNTs we have reported so far are for an average over metallic and semiconducting CNTs. Our results agree well with those reported in [49], despite the different substrate and diameters of the nanotube samples. This confirms that there is no obvious dependence on environment or diameter for the range of our investigations.

4.2.4 Anti-Stokes Raman blue shift

In addition to the changes in the decay rate of the G-mode phonons with the initial temperature (Figure 4.5), a time dependence in the G-mode energy shift (see Figure 4.6b adapted from [59]) is also observed for measurements in graphite. In particular, an increase of the optical phonon frequencies with the pump excitation of the sample has been observed. The shorter the

delay time between the pump and the probe pulses, the higher the frequency of the G-mode phonons.

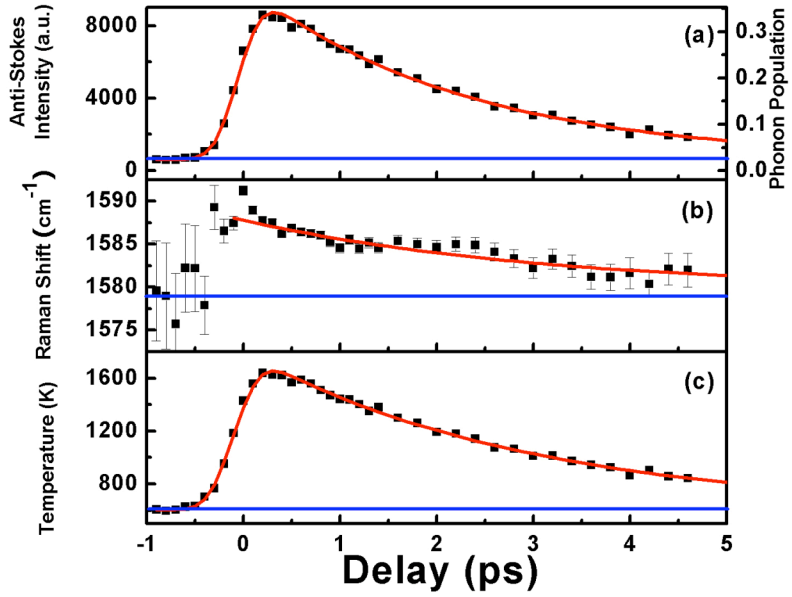

Figure 4.6 The G-mode phonons time evolution adapted from [59] is depicted. (a) The anti-Stokes signal intensity from the non-equilibrium phonons is shown on the left axis and the corresponding phonon population on the right axis. The data are fitted with an exponential decay function with time constant of 2.2 ps, convolved with the response function of the instrument (shown in red). (b) The shift of the energy of the phonons as a function of delay time. The blue line represents the Raman signal in the absence of the pump beam. (c) The inferred evolution of the phonon and electronic temperature as a function of delay time.

By using the phonon population n (shown in Figure 4.6a), their temperature evolution (Figure 4.6c) has been derived. This is in turn used to study the Raman shift as a function of the transient phonon temperature T (Figure 4.7). The observed shift is about 8 cm^{-1}.

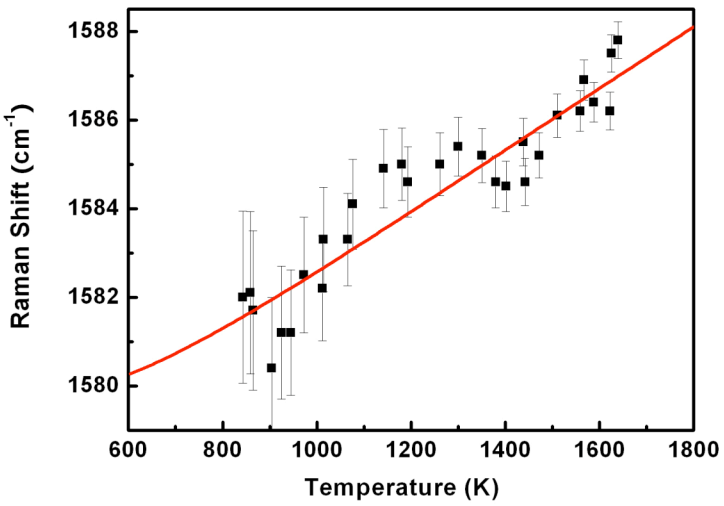

Figure 4.7 Observed blue shift of the G-mode optical phonons versus the transient phonon temperature (adapted from [59]). The shift is attributed to a corresponding change in the electronic temperature, which leads to a shift in the phonon frequency similar to that observed for electrostatic doping [63,64].

The blue shift of the energy of the phonons under pump excitation can be understood qualitatively in terms of Kohn anomaly. Kohn showed that metals may have singularities in their phonon dispersion with $\left|\nabla_{\mathbf{q}}\omega(\mathbf{q})\right| = \infty$ [68] due to strong coupling between electrons and phonons for particular values of the phonon wave vector $\mathbf{q}$. The Kohn anomaly occurs at $\mathbf{q} = \mathbf{k}_2 - \mathbf{k}_1$ with the phonon having the correct symmetry to couple the electrons at the Fermi energy. In graphene the Fermi surface is a single point, hence in the limit $\mathbf{k}_2 \rightarrow \mathbf{k}_1$ a Kohn anomaly is anticipated at $q = 0$. For $q = K$, which is the wave vector which connects K, K', a second anomaly occurs. Similar qualitative behavior is expected for graphite. For those wave vectors and phonon symmetries, the electron phonon coupling can generate distortions in the lattice known as Peirels distortions [69,70]. This effect in turn leads to a reduction of the energy of the system due to the fact that a gap in the Fermi energy has been opened up. In the region of such an anomaly, the dispersion relation becomes linear with a slope proportional to the electron-phonon coupling. Thus, changes

in the electron-phonon coupling will alter the Kohn anomaly and, hence, the phonon frequency [59].

We can model the energy blue shift of the optical phonons more quantitative using the concept of the phonon self-energy [33,65]. Following Ando's [66] analysis for the graphene band structure, we have for the phonon-self energy

$$\Pi = \lim_{\delta \to 0} \left\{ -\lambda \int_0^{+\infty} \varepsilon d\varepsilon [f_T(-\varepsilon) - f_T(\varepsilon)] \times \left(\frac{1}{\hbar\omega_G + 2\varepsilon + i\delta} - \frac{1}{\hbar\omega_G - 2\varepsilon + i\delta} \right) \right\} \qquad (4.2)$$

where ε is the difference between the initial and the final state of the electron and $\hbar\omega_G$ is the energy of the phonon. The $f_T(\varepsilon)$ is the Fermi-Dirac distribution functions [66]. The real part represents the energy shift (Figure 4.7) and the imaginary $\mathrm{Im}\{\Pi\}$ the lifetime of the phonon. The data have been fitted with equation (4.2) by taking into account only the points which correspond to delay times larger than 200 fs, so that the equilibrium between the electronic gas and phonons can be established. From the slope of the line one can find the electron-phonon coupling parameter λ.

In summary, we have directly measured the temperature dependence of the anharmonic decay rate, $\Gamma_{ph\text{-}ph}(T)$, for the zone-center (G-mode) optical phonons in graphite and nanotubes by time-resolved Anti-Stokes Raman scattering. We find that $1/\Gamma_{ph\text{-}ph}(T)$ varies from (a) 1.23 ± 0.15 ps to 0.75 ± 0.15 ps for the temperature range 6 K to 512 K for SWNT, and (b) 1.92 ± 0.02 ps to 1.27 ± 0.05 ps for the temperature range 340 K to 685 K for graphite. Both of these decay rates are somewhat faster than predicted theoretically by Bonini *et al.* [61]. The temperature dependence of the decay rate, $\Gamma_{ph\text{-}ph}(T)$, in graphite agrees well with theory, and we find that two decay channels TA-LA contribute most to the decay rate. However, the rate $\Gamma_{ph\text{-}ph}(T)$ in SWNT increases faster than theory predicts for graphene. This suggests the presence of additional decay channels involving low-frequency modes, such as the RBM, pinch and bending modes. Higher anharmonic decay rates suggest that non-equilibrium phonons may be more difficult to generate

than previously predicted. A blue shift of the optical phonons of about 8 cm^{-1} under the pump influence has also been observed for graphite. We anticipate the same effect for the SWNTs.

CHAPTER 5 - Conclusions

In this dissertation the ultrafast dynamics of electrons and phonons in graphitic materials has been studied.

By using time-resolved Two-Photon photoemission (TR-TPP) spectroscopy we probe the dynamics of optically excited charge carriers above the Fermi energy of double-wall carbon nanotubes (DWNTs). In particular, we found:

- At long delay time (i.e., 570 fs) after the excitation, an equilibrium has been established between the electrons and phonons, and the Fermi-Dirac function describes well the experimental data (Figure 3.10).

- The energy of the electronic gas decays exponentially towards the lattice with a time constant of ~1.52 ± 0.76 ps (Figure 3.11).

- The energy transfer rate exhibits a rapid non-linear growth with temperature see (Figure 3.12).

- An electron-phonon mass enhancement parameter of $\lambda = (1.16 \pm 0.16) \times 10^{-4}$.

- An electron scattering mean free path of ~25 ± 1 μm.

The above results are described in Chatzakis *et al.* (2009a; to be submitted).

We also applied time-resolved anti-Stokes Raman spectroscopy to study the optically excited zone-center (G-mode) non-equilibrium optical phonon population in single-wall carbon

nanotubes (SWNTs) and graphite in a wide temperature range. In particular, we measured the energy relaxation rate due to anharmonic interactions between the phonons from 6 K to 515 K for SWNTs and from 340 K to 685 K for graphite and we found:

- Decay times of 1.23 ± 0.15 ps at 6 K and 0.75 ± 0.15 ps at 515 K for SWNTs, and 1.92 ± 0.02 ps at 340 K and 1.27 ± 0.05 ps at 685 K for graphite.

- Results consistent with previous studies at room temperature for both samples, i.e., 1.1 ± 0.1 ps for SWNTs and 2.2 ± 0.1 ps [59] for graphite, respectively.

- The frequencies of the decay phonons ω_1 and ω_2 to be 396 cm^{-1} and 1189 cm^{-1} with an anharmonic constant of 0.82 ± 0.05 ps^{-1} for SWNTs. For graphite we found ω_1 and ω_2 equal to 539 cm^{-1} and 1046 cm^{-1} and an anharmonic constant of 0.47 ± 0.05 ps^{-1}.

- The $\Gamma_{ph\text{-}ph}$ rate in graphite agrees well with theory [61].

- Two decay channels TA-LA contribute the most to the decay rate.

- The $\Gamma_{ph\text{-}ph}$ rate in SWNTs increases faster than theory predicts for graphene [61], thus suggesting the presence of additional decay channels involving low-frequency modes, such as RBM, pinch and bending modes.

- An increase of the optical G-mode phonons energy decay rate with temperature (see Figure 4.5), which behaves linearly above room temperature.

- An increase in the energy of the G-mode optical phonons in graphite with the transient temperature.

These results are described in Chatzakis *et al.* (to be submitted), and Yan *et al*. (2008; PRL submitted).

CHAPTER 6 - Bibliography

1. S. Iijima. Helical microtubules of graphitic carbon. *Nature* **354**, 56 (1991).

2. K. S. Novoselov, A. K. Geim, S. V. Morozov, D. Jiang, Y. Zhang, S. V. Dubonos, I.V. Grigorieva and A. A. Firsov. Electric Field Effect in Atomically Thin Carbon Films. *Science* **306**, 666 (2004).

3. K. S. Novoselov, A. K. Geim, S. V. Morozov, D. Jiang, M. I. Katsnelson, I. V. Grigorieva, S. V. Dubonos and A. A. Firsov. Two-dimensional gas of massless Dirac fermions in graphene. *Nature* **438**, 197 (2005).

4. P. Avouris, Z. Chen and V. Perebeinos. Carbon-based electronics. *Nature Nanotech.* **2**, 605 (2007).

5. S. Reich, C. Thomsen and J. Maultzsch. *Carbon Nanotubes - Basic Concepts and Physical Properties*, Ed. WILEY-VCH Verlag GmbH & Co. KGaA, (Weinheim, 2004).

6. C. Thomsen and S. Reich. *Raman Scattering in Carbon Nanotubes*, in *Light Scattering in Solids IX (Topics in Applied Physics 108)*. Eds. M. Cardona and R. Merlin, Springer-Verlag, p. 115 (Berlin, 2007).

7. T. G. Pedersen. Analytic calculation of the optical properties of graphite. *Phys. Rev. B* **67**, 113106 (2003).

8. T. Kampfrath, L. Perfetti, F. Schapper, C. Frischkorn and M. Wolf. Strongly Coupled Optical Phonons in the Ultrafast Dynamics of the Electronic Energy and Current Relaxation in Graphite. *Phys. Rev. Lett.* **95**, 187403 (2005).

9. E. N. Economou. *Solid State Physics*, Crete University Press, (Crete, Greece 1997).

10. J. W. Mintmire and C. T. White. Universal Density of States for Carbon Nanotubes. *Phys. Rev Lett.* **81**, 2506 (1998).

11. F. Wang, G. Dukovic, L. E. Brus and T. F. Heinz. The Optical Resonances in Carbon Nanotubes Arise from Excitons. *Science* **308**, 838 (2005).

12. Z. Yao, C. L. Kane and C. Dekker. High-Field Electrical Transport in Single-Wall Carbon Nanotubes. *Phys. Rev. Lett.* **84**, 2941 (2000).

13. A. Loiseau, P. Launois, P. Petit, S. Roche and J. P. Salvetat. *Understanding Carbon Nanotubes: From Basics to Applications* (Lecture Notes in Physics 677), Eds. A. Loiseau, P. Launois, P. Petit, S. Roche and J.-P. Salvetat, Springer –Verlag (Berlin Heidelberg, 2006).

14. P. B. Allen. Theory of thermal relaxation of electrons in metals. *Phys. Rev. Lett.* **59**, 1460 (1987).

15. A. Hagen, G. Moos, V. Talalaev and T. Hertel. Electronic structure and dynamics of optically excited singe-wall carbon nanotubes. *Appl. Phys. A* **78**, 1137 (2004).

16. T. Hertel, R. Fasel and G. Moos. Charge-carrier dynamics in single-wall carbon nanotube bundles: a time-domain study. *Appl. Phys. A* **75**, 449 (2002).

17. M. Zamkov, A. Alnaser, B. Shan, Z. Chang and P. Richard. Probing the intrinsic conductivity of multiwalled carbon nanotubes. *Appl. Phys. Lett.* **89**, 093111 (2006).

18. E. Knosel. Dynamics of photoexcited electrons in metals studied with time-resolved two-photon photoemission. *Surface Science* **368**, 76 (1996).

19. D. Panes and P. Nozières. *The theory of quantum liquids: Volume I*, Ed. W. A. Benjamin, Inc. (New York, 1966).

20. Y. Uehara, T. Ushiroku, S. Ushioda and Y. Murata. High resolution Time-of-flight electron spectrometer. *Jap. J. of Appl. Phys*. **29**, 2858 (1990).

21. E. Mazur. *Interaction of ultrashort laser pulses with solids.* Ed. B. Di Bartolo (Plenum, NATO ASI series, 1996).

22. P. A. Loukakos. *The influence of structure on ultrafast electron dynamics in non-stoichiometric III-V semiconductors and metallic nano composites.* PhD thesis: University of Crete, Physics Department (2002).

23. J. Jiang, R. Saito, A. Grüneis, S. G. Chou, Ge. G. Samsonidze, A. Jorio, G. Dresselhaus and M. S. Dresselhaus. Photoexcited electron relaxation processes in single-wall carbon nanotubes. *Phys. Rev. B* **71**, 045417 (2005).

24. T. Nihira and T. Iwata. Temperature dependence of lattice vibrations and analysis of the specific heat of graphite. *Phys. Rev. B* **68**, 134305 (2003).

25. S. I. Anisimov, B. L. Kapeliovich and T. L. Perel'Man. Electron emission from metal surfaces exposed to ultrashort laser pulses. *Sov. Phys. JETP* **39**, 375 (1974).

26. G. Moos, R. Fasel and T. Hertel. Temperature Dependence of Electron to Lattice Energy-Transfer in Single-Wall Carbon Nanotube Bundles. *J. Nanosci Nanotech.* **3**, 145 **(**2003).

27. R. H. M. Groeneveld, R. Sprik and A. Langendijk. Femtosecond spectroscopy of electron-electron and electron-phonon energy relaxation in Ag and Au. *Phys. Rev. B* **51**, 11433 (1995).

28. T. Hertel and G. Moos. Electron-Phonon Interaction in Single-Wall Carbon Nanotubes: A Time-Domain Study. *Phys. Rev. Lett.* **84**, 5002 (2000).

29. E. Pop, D. Mann, J. Cao, Q. Wang, K. Goodson and H. Dai. Negative Differential Conductance and Hot Phonons in Suspended Nanotube Molecular Wires. *Phys. Rev. Lett.* **95**, 155505 (2005).

30. H. Petek and S. Ogawa. Femtosecond Time-Resolved Two-Photon Photoemission Studies of Electron Dynamics in Metals. *Prog. in Surface Science* **56**, 239 (1997).

31. G. D. Mahan. *Many-particle Physics*, 3rd edition, Ed. Kluwer Academic / Plenum Publishers, p. 531 (New York, 2000).

32. B. K. Bhattacharyya and J. C. Swihart. Calculation of the anisotropy of the electron-phonon mass-enhancement parameter and the cyclotron mass in indium. *J. Phys. F: Met. Phys.* **14**, 1651 (1984).

33. G. Grimvall. *The electron-phonon interaction in metals.* Volume XVI, Ed. E. P. Wohlfarth, North-Holland, p. 102 (Netherlands, 1981).

34. M. Bockrath, D. H. Cobden, J. Lu, A. G. Rinzler, R. E. Smalley, L. Balents and P. L. McEuen. Luttinger-liquid behaviour in carbon nanotubes. *Nature* **397**, 598 (1999).

35. F. Wang, G. Dukovic, L. E. Brus and T. F. Heinz. The Optical Resonances in Carbon Nanotubes Arise from Excitons. *Science* **308**, 838 (2005).

36. J. Maultzsch, R. Pomraenke, S. Reich, E. Chang, D. Prezzi, A. Ruini, E. Molinari, M. S. Strano, C. Thomsen and C. Lienau. Exciton binding energies in carbon nanotubes from two-photon photoluminescence. *Phys. Rev. B* **72**, 241402 (2005).

37. V. Perebeinos, J. Tersoff and P. Avouris. Effect of Exciton-Phonon Coupling in the Calculated Optical Absorption of Carbon Nanotubes. *Phys. Rev. Lett.* **94**, 027402 (2005).

38. J.-Y. Park, S. Rosenblatt, Y. Yaish, V. Sazonova, H. Üstünel, S. Braig, T. A. Arias, P. W. Brouwer and P. L. McEuen. Electron−Phonon Scattering in Metallic Single-Walled Carbon Nanotubes. *Nano Letters* **4**, 517 (2004).

39. S. G.F. Plentz, J. Jiang, R. Saito, D. Nezich, H. B. Ribeiro, A. Jorio, M. A. Pimenta, Ge. G. Samsonidze, A. P. Santos, M. Zheng, G. B. Onoa, E. D. Semke, G. Dresselhaus and M. S. Dresselhaus. Phonon-Assisted Excitonic Recombination Channels Observed in DNA-Wrapped Carbon Nanotubes Using Photoluminescence Spectroscopy. *Phys. Rev. Lett.* **94**, 127402 (2005).

40. Z. Yao, C. L. Kane and C. Dekker. High-Field Electrical Transport in Single-Wall Carbon Nanotubes. *Phys. Rev. Lett.* **84**, 2941 (2000).

41. V. Perebeinos, J. Tersoff, J. and P. Avouris. Electron-Phonon Interaction and Transport in Semiconducting Carbon Nanotubes. *Phys. Rev. Lett.* **94**, 086802 (2005).

42. M. Lazzeri, S. Piscanec, F. Mauri, A. C. Ferrari and J. Robertson. Electron Transport and Hot Phonons in Carbon Nanotubes. *Phys. Rev. Lett.* **95**, 236802 (2005).

43. M. Lazzeri and F. Mauri. Coupled dynamics of electrons and phonons in metallic nanotubes: Current saturation from hot-phonon generation. *Phys. Rev. B* **73**, 165419 (2006).

44. A. Javey, J. Guo, M. Paulsson, Q. Wang, D. Mann, M. Lundstrom and H. Dai. High-Field Quasiballistic Transport in Short Carbon Nanotubes. *Phys. Rev. Lett.* **92**, 106804 (2004).

45. A. Jorio, C. Fantini, M. S. Dantas, M. A. Pimenta, F. A. G. Souza, Ge. G. Samsonidze, V. W. Brar, G. Dresselhaus, M. S. Dresselhaus, A. K. Swan, M. S. Ünlü, B. B. Goldberg and R. Saito. Linewidth of the Raman features of individual single-wall carbon nanotubes. *Phys. Rev. B* **66**, 115411 (2002).

46. N. R. Raravikar, P. Keblinski, A. M. Rao, M. S. Dresselhaus, L. S. Schadler and P. M. Ajayan. Temperature dependence of radial breathing mode Raman frequency of single-walled carbon nanotubes. *Phys. Rev. B* **66**, 235424 (2002).

47. J. A. Kash, J. C. Tsang and J. M. Hvam. Sub-picosecond time-resolved Raman spectroscopy of LO phonons in GaAs. *Phys. Rev. Lett.* **54**, 2151 (1985).

48. D. Song, F. Wang, G. Dukovic, M. Zheng, E. D. Semke, L. E. Brus and T. F. Heinz. Direct Measurement of the Lifetime of Optical Phonons in Single-Walled Carbon Nanotubes. *Phys. Rev. Lett.* **100**, 225503 (2008).

49. K. Kang, T. Ozel, D. G. Cahill and M. Shim. Optical Phonon Lifetimes in Single-Walled Carbon Nanotubes by Time-Resolved Raman Scattering. *Nano Lett.* **8**, 4642 (2008).

50. A. Debernardi. Phonon linewidth in III-V semiconductors from density-functional perturbation theory. *Phys. Rev. B* **57**, 12847 (1998).

51. J. Menéndez and M. Cardona. Temperature dependence of the first-order Raman scattering by phonons in Si, Ge, and α-Sn: Anharmonic effects. *Phys. Rev. B* **29**, 2051 (1984).

52. M. Balkanski, R. F. Wallis and E. Haro. Anharmonic effects in light scattering due to optical phonons in silicon. *Phys. Rev. B* **28**, 1928 (1983).

53. F. Vallée. Time-resolved investigation of coherent LO-phonon relaxation in III-V semiconductors. *Phys. Rev. B* **49**, 2460 (1994).

54. A. Gambetta, C. Manzoni, E. Menna, M. Meneghetti, G. Cerullo, G. Lanzani, S. Tretiak, A. Piryatinski, A. Saxena, R. L. Martin and A. R. Bishop. Real-time observation of nonlinear coherent phonon dynamics in single-walled carbon nanotubes. *Nature Physics* **2**, 515 (2006).

55. F. Wang, G. Dukovic, E. Knoesel, L. E. Brus and T. F Heinz. Observation of rapid Auger recombination in optically excited semiconducting carbon nanotubes. *Phys. Rev. B* **70**, 241403 (2004).

56. T. G. Pedersen. Analytic calculation of the optical properties of graphite. *Phys. Rev. B* **67**, 113106 (2003).

57. H.-G. Rubahn. *Laser Applications in Surface Science and Technology*, Ed. John Wiley & Sons Ltd (England, 1999).

58. P. G. Klemens. Anharmonic Decay of Optical Phonons. *Phys. Rev.* **148**, 845 (1966).

59. H. Yan, D. Song, K. F. Mak, I. Chatzakis, J. Maultzsch and T. F. Heinz. Probing non-equilibrium Phonon Dynamics in Graphite by Time-Resolved Raman spectroscopy. *Phys. Rev. Lett.* (submitted; 2008).

60. A. Debernardi. Anharmonic effects in the phonons of III-V semiconductors: first principles calculations. *Solid State Comm.* **113**, 1 (1999).

61. N. Bonini, M. Lazzeri, N. Marzari and F Mauri. Phonon Anharmonicities in Graphite and Graphene. *Phys. Rev. Lett.* **99**, 176802 (2007).

62. G. P. Srivastava. *The physics of phonons*, Taylor & Francis Group, LLC, (New York, 1990).

63. J. C. Tsang, M. Freitag, V. Perebeinos, J. Liu and P. Avouris. Doping and phonon renormalization in carbon nanotubes. *Nature Nanotech.* **2**, 725 (2007).

64. J. Yan, Y. Zhang, P. Kim and A. Pinczuk. Electric Field Effect Tuning of Electron-Phonon Coupling in Graphene. *Phys. Rev. Lett.* **98**, 166802 (2007).

65. G. D. Mahan. *Many-particle Physics*, 3rd edition, Kluwer Academic / Plenum Publishers, p. 487 (New York, 2000).

66. T. Ando. Anomaly of Optical Phonon in Monolayer Graphene. *J. Phys. Soc. Jpn*. **75,** 124701 (2006).

67. G. Grimvall. New aspects on the elecron-phonon system at finite temperatures with an application on Lead and Mercury. *Phys. Kondens. Materie* **9**, 283 (1969).

68. W. Kohn. Image of the Fermi Surface in the Vibration Spectrum of a Metal. *Phys. Rev.* **2**, 393 (1959).

69. K. -P. Bohnen, R. Heid, H. J. Liu and C. T. Chan. Lattice Dynamics and Electron-Phonon Interaction in (3,3) Carbon Nanotubes. *Phys. Rev. Lett.* **93**, 245501 (2004).

70. D. Connétable, G. -M. Rignanese, J. -C. Charlier and X. Blasé. Room Temperature Peierls Distortion in Small Diameter Nanotubes. *Phys. Rev. Lett.* **94**, 015503 (2005).

71. G. Grimvall. *The electron-phonon interaction in metals.* Volume XVI, Ed. E. P. Wohlfarth, North-Holland, p. 107 (Netherlands, 1981).

72. M. Zamkov, N. Woody, B. Shan, Z. Chang and P. Richard. Lifetime of Charge Carriers in Multiwalled Nanotubes. *Phys. Rev. Lett.* **94**, 056803 (2005).

73. A. G. Walsh. *Exciton behavior in carbon nanotubes: dielectric screening and decay dynamics.* PhD thesis: Boston University (2009).

74. C. Berger, Y. Yi, Z. L. Wang and W. A. de Heer. Multiwalled carbon nanotubes are ballistic conductors at room temperature. *Appl. Phys. A* **74**, 363 (2002).

Appendix A - Electronic energies for graphene and graphite

Table A.1 Electronic energies of graphite and graphene for the π and σ states at high symmetry points. The differences between the calculated and measured values are mostly due to the differences between graphene and graphite.

	Valence (eV)			Conduction (eV)		
	Γ	M	K	Γ	M	K
Graphite (experiment)						
π	-8.8	-1.8	-0.2	12.2	2.2	0.46
		-2.6	-0.8		2.9	
	-7.9	-3.1	-0.57			
σ	-4.0	-6.4	-10.3	7.5	8.6	14.7
		-11.8	-11.3			
		-16.3				
	-4.2	-7.8	-11.7			
	-21.8	-16.7	-14.4			
Graphene (calculation)						
π	-7.67	-2.35	0.0	11.45	1.66	0.0
σ		-6.44	-10.6		7.56	12.8
	-3.05			8.33		
		-13.2			12.8	19.9
	-19.3	-14.0				

* All the information contained in this page has been adopted from [5].

Appendix B - Mass enhancement parameter

The parameter λ is a factor by which the effective mass of an electron is changed due to electron-phonon interactions. and it is given by the following equation

$$\lambda = 2\int_0^{\omega_D} \frac{\alpha^2 F(\omega)}{\omega} d\omega \qquad \text{B.1}$$

where $\alpha^2 F(\omega)$ is the Eliashberg electron-phonon coupling function with

$$F(\omega) = \sum_\sigma \int \frac{d^3 q}{(2\pi)^3} \delta(\omega - \omega_\sigma(\mathbf{q})) \qquad \text{B.2}$$

being the phonon density of states and α^2 the electron-phonon coupling. The Eliashberg function is given by

$$\alpha^2 F(\omega) = \frac{1}{(2\pi)^3} \int_{FS} \frac{dS'}{\upsilon(\mathbf{k})} \sum_\sigma \left| g_{\mathbf{k}\mathbf{k}'\sigma} \right|^2 \delta(\omega - \omega_{\mathbf{q}\sigma}) \qquad \text{B.3}$$

In equation B.3, $g_{\mathbf{k}\mathbf{k}'\sigma}$ is the electron-phonon coupling matrix element for scattering from one electronic state **k** to another **k′** with the emission of a phonon of wavevector **q**, polarization σ and group velocity υ(**k**). The $\alpha^2 F(\mathbf{k},\omega)$ can be thought as a total transition probability from one electronic state to another with the contribution of a phonon, while the wavevector **q** satisfies the momentum conservation condition.

The relation which then describes the increase of the effective mass is

$$m^* = m_0(1+\lambda) \qquad \text{B.4}$$

where m_0 is the effective mass without electron-phonon coupling.